Mysteriously high Δ^{14}C of the glacial atmosphere: Influence of ^{14}C production and carbon cycle changes

Ashley Dinauer[1,*], Florian Adolphi[1,2], Fortunat Joos[1]

[1]Climate and Environmental Physics, Physics Institute and Oeschger Centre for Climate Change Research, University of Bern, Sidlerstrasse 5, 3012 Bern, Switzerland

[2]Quaternary Sciences, Department of Geology, Lund University, Sölvegatan 12, 22362 Lund, Sweden

*To whom correspondence should be addressed. Email: ashley.dinauer@climate.unibe.ch

Abstract. Despite intense focus on the ~190 permil drop in atmospheric Δ^{14}C during Heinrich Stadial 1 ~17.4 to 14.6 kyr BP, the specific mechanisms responsible for the apparent Δ^{14}C excess in the glacial atmosphere have received considerably less attention. The computationally efficient Bern3D earth system model of intermediate complexity, designed for long-term climate simulations, allows us to address a very fundamental but still elusive question concerning the atmospheric Δ^{14}C record: How can we explain the persistence of relatively high Δ^{14}C values during the millennia after the Laschamp event? Large uncertainties in the pre-Holocene ^{14}C production rate, as well as in the older portion of the Δ^{14}C record, complicate our qualitative and quantitative interpretation of the glacial Δ^{14}C elevation. Here we begin with sensitivity experiments that investigate the controls on atmospheric Δ^{14}C in idealized settings. We show that the interaction with the ocean sediments may be much more important to the simulation of Δ^{14}C than had been previously thought. In order to provide a bounded estimate of glacial Δ^{14}C change, the Bern3D model was integrated with five available estimates of the ^{14}C production rate as well as reconstructed and hypothetical paleoclimate forcing. Model results demonstrate that none of the available reconstructions of past changes in ^{14}C production can reproduce the elevated Δ^{14}C levels during the last glacial. In order to increase atmospheric Δ^{14}C to glacial levels, a drastic reduction of air-sea exchange efficiency in the polar regions must be assumed, though discrepancies remain for the portion of the record younger than ~33 kyr BP. We end with an illustration of how the ^{14}C production rate would have had to evolve to be consistent with the Δ^{14}C record, by combining an atmospheric radiocarbon budget with the Bern3D model. The overall conclusion is that the remaining discrepancies with respect to glacial Δ^{14}C may be linked to an underestimation of ^{14}C production and/or a biased-high reconstruction of Δ^{14}C over the time period of interest. Alternatively, we appear to still be missing an important carbon cycle process for atmospheric Δ^{14}C.

1 Introduction

The cosmogenic radionuclide radiocarbon (^{14}C) is a powerful tracer for the study of several ocean processes including deep ocean circulation and ventilation. Past changes in atmospheric ^{14}C/C (i.e., Δ^{14}C$_{atm}$, in permil; corresponding to Δ from Stuiver and Polach, 1977), as recorded in absolutely dated tree rings, plant macrofossils, speleothems, corals,

37 and foraminifera, have been interpreted as possibly reflecting real changes in the ocean's large-scale overturning
38 circulation (Siegenthaler et al., 1980). The extended 54,000-year record of $\Delta^{14}C_{atm}$ from the latest IntCal compilation
39 (i.e., IntCal13; Reimer et al., 2013) and from two Hulu Cave stalagmites (Cheng et al., 2018) suggests that large
40 millennial-scale variations in $\Delta^{14}C_{atm}$ have occurred during the last glacial, compared to the relatively small (~30 ppm)
41 change in atmospheric CO_2 over the same time period (Fig. 1). When interpreting the implications of such changes, it
42 is important to note that $\Delta^{14}C_{atm}$ is controlled not only by global carbon cycle processes but also by variations in the
43 atmospheric ^{14}C production rate. Therefore, the use of $\Delta^{14}C_{atm}$ as an indicator of past oceanic conditions, particularly
44 those associated with air-sea exchange efficiency and deep ocean ventilation rates, requires reliable estimates of the
45 ^{14}C production rate over time.
46
47   The vast majority of all ^{14}C production changes are the result of either solar or geomagnetic modulation of
48 the cosmic ray flux reaching the Earth (Masarik and Beer, 1999; Poluianov et al., 2016). Fig. 1 shows several different
49 proxy records of the global production rate of ^{14}C in relative units covering the full range of the ^{14}C dating method,
50 based on geomagnetic field data from marine sediments (Laj et al., 2000; Laj et al., 2004; Nowaczyk et al., 2013;
51 Channell et al., 2018) and on ^{10}Be and ^{36}Cl measurements in polar ice cores (Adolphi et al., 2018). A fundamental
52 difference between these reconstruction methods is that paleointensity-based estimates of the ^{14}C production rate, by
53 definition, do not reflect changes in the solar modulation of the cosmic radiation, whereas ice-core ^{10}Be-based
54 estimates give the combined influence of solar and geomagnetic modulation on radionuclide production. Of note is
55 the striking coherence in all three records $\Delta^{14}C_{atm}$, paleointensity-based production, and ice-core ^{10}Be-based
56 production) of the Laschamp excursion (~41 kyr BP), when the Earth's geomagnetic dipole field briefly reversed and
57 its intensity was close to zero (Nowaczyk et al., 2012; Laj et al., 2014). According to reconstructions and production
58 rate models, this large geomagnetic event caused a doubling of the ^{14}C production rate, leading to the highest $\Delta^{14}C_{atm}$
59 values over the last 54 kyr. Relatively high $\Delta^{14}C_{atm}$ values continued until ~25 kyr BP, then gradually diminished to
60 preindustrial levels, interrupted by a sharp drop in $\Delta^{14}C_{atm}$ during Heinrich Stadial 1 (HS1) ~17.4 to 14.6 kyr BP
61 (sometimes called the "mystery interval"; Broecker and Barker, 2007). While the Laschamp geomagnetic excursion
62 appears to be responsible for the $\Delta^{14}C_{atm}$ peak at ~41 kyr BP, the production rate estimates during much of the pre-
63 Holocene period are subject to considerable uncertainty.
64
65   Paleointensity-based reconstructions are sensitive to coring disturbances of poorly consolidated sediments.
66 The last 50 kyr are represented by the relatively slushy uppermost few meters of recovered marine sediment cores
67 (Channell et al., 2018). Channell et al. (2018) preferentially selected cores recovered using conventional piston and
68 square barrel gravity coring methods, and from sites with high mean (> 15 cm kyr^{-1}) sedimentation rates, so as to
69 minimize the influence of drilling disturbance, and reached very different production rates than, e.g., Laj et al. (2000).
70 On the other hand, ice-core ^{10}Be records are affected by changes in the transport and deposition of atmospheric ^{10}Be,
71 which may overprint the production rate changes (e.g., Heikkilä et al., 2013). Furthermore, in order to calculate the
72 ice-core ^{10}Be deposition fluxes, snow accumulation rates must be known for each specific ice core, which themselves
73 have uncertainties on the order of 10 to 20 percent that propagate into the ice-core ^{10}Be fluxes (Gkinis et al., 2014;

74 Rasmussen et al., 2013). The large uncertainties associated with the reconstruction of past changes in ^{14}C production

75 hamper our ability to predict reliably the extent to which production changes contributed to high glacial $\Delta^{14}C_{atm}$ levels.

76 Only if estimates of past changes in ^{14}C production are robust can one improve assessments of the relative importance

77 of the two fundamental mechanisms responsible for glacial-interglacial $\Delta^{14}C$ changes: (1) production changes and (2)

78 carbon cycle changes.

79

80   Earlier model studies have focused heavily on the ~190 permil drop in $\Delta^{14}C_{atm}$ during HSI and on the deglacial

81 trends in $\Delta^{14}C_{atm}$ after HS1 (Muscheler et al., 2004; Broecker and Barker, 2007; Skinner et al., 2010; Mariotti et al.,

82 2016; Delaygue et al., 2003; Marchal et al., 2001; Huiskamp and Meissner, 2012; Hain et al., 2014). Historically, the

83 younger portion of the $\Delta^{14}C_{atm}$ record has received more attention than the glacial section because of the early emphasis

84 on the general climatic trends of the North Atlantic stadials (HS1 and the Younger Dryas [YD]) and the Bølling-

85 Allerød (BA) warm period, and on the important role of an exceptionally aged (^{14}C-depleted) deep-water mass in the

86 pulsed rise of atmospheric CO_2 during the last glacial termination (e.g., Skinner et al., 2017). Less research over the

87 last few decades has studied the specific mechanisms responsible for high glacial $\Delta^{14}C_{atm}$ levels. The model studies

88 that are available point out the difficulties in simulating the correct glacial $\Delta^{14}C_{atm}$ levels (Hughen et al., 2004; Köhler

89 et al., 2006). These studies demonstrate with box models that glacial levels of $\Delta^{14}C_{atm}$ cannot be attained without

90 invoking significant changes in ocean circulation, air-sea gas exchange, and carbonate sedimentation. However, the

91 box models were not able to reproduce $\Delta^{14}C_{atm}$ values higher than 700 permil, and these results still need to be

92 scrutinized with models of higher complexity. To our knowledge, no three-dimensional ocean biogeochemical model

93 has yet simulated the 50,000-year record of $\Delta^{14}C_{atm}$. Many questions remain unanswered, in particular: What

94 mechanism can account for the persistence of relatively high $\Delta^{14}C_{atm}$ values during the millennia after the Laschamp

95 excursion?

96

97   The expected time scale for sustaining elevated levels of $\Delta^{14}C_{atm}$ after a production peak is on the order of

98 thousands of years, a time scale tied to the mean lifetime of ^{14}C (~8223 years; Audi et al., 2003; Bé et al., 2013) and

99 the time required for deep ocean ventilation (on the order of 1000 years or more; Primeau, 2005). Specifically,

100 Muscheler et al. (2004) demonstrate that the characteristic time constant for equilibration of $\Delta^{14}C_{atm}$ after a

101 perturbation in atmospheric production is 5000 years. By this analysis, the Laschamp event, which lasted only about

102 1500 to 2000 years (Laj et al., 2000), was insufficient to sustain the high $\Delta^{14}C_{atm}$ values observed over the next ~15,000

103 years. The lack of significant changes (only ~10 percent) in atmospheric CO_2 during the time period of interest raises

104 the question of what causes variations in $\Delta^{14}C_{atm}$, but not CO_2, on millennial time scales? The obvious answers are:

105 cosmic ray modulation and air-sea gas exchange. Ultimately, no explanation for high glacial $\Delta^{14}C_{atm}$ levels can be

106 complete in the absence of more robust estimates of the pre-Holocene ^{14}C production rate, as well as a good

107 understanding of the ocean carbon cycle under glacial climate conditions.

108

109   One of the major challenges associated with modelling glacial-interglacial climate cycles is that it is currently

110 not possible to reproduce climate and atmospheric CO_2 variations on the basis of orbital forcing alone. Problems

include the complexity of the Earth system, making it difficult to represent all the relevant processes in models, and the long time scales involved, making simulations covering tens of thousands of years costly in computation time. Glacial-interglacial simulations with dynamic ocean and land models of intermediate complexity have begun to emerge, but these models are not yet able to reproduce the reconstructed variations in important proxy data or the timing of CO_2 variations during the last glacial termination (Brovkin et al., 2012; Ganopolski and Brovkin, 2017; Menviel et al., 2012). A wide variety of mechanisms, both physical and biological, centered on or connected with the ocean, as well as exchange processes with the land biosphere, marine sediments, coral reefs, and the lithosphere, are thought to play a role in explaining the glacial-interglacial variations in atmospheric CO_2 (Archer et al., 2000; Fischer et al., 2010; Wallmann et al., 2016; Galbraith and Skinner, 2020), but how they interacted over time under the influence of orbital forcing remains elusive. We appear to still be missing a single framework in which these mechanisms are linked to each other in a predictable manner. As long as there are still large gaps in our understanding of the glacial climate and associated ocean carbon cycle, a convenient way to examine the impact of the possible mechanisms on atmospheric CO_2 levels, and here on $\Delta^{14}C_{atm}$, is to perform sensitivity experiments and scenario-based simulations with models. This allows us to investigate specific phenomena in idealized settings, permitting us to investigate in detail which parameters and processes are most important in controlling $\Delta^{14}C_{atm}$ levels.

In this paper we extend previous modelling efforts concerning the record of $\Delta^{14}C_{atm}$ with respect to three issues: (1) the sensitivity of the $\Delta^{14}C_{atm}$ response to carbon cycle changes and the potential importance of marine sediments, (2) the simulation of $\Delta^{14}C_{atm}$ covering the time range of the IntCal13 radiocarbon calibration curve (50,000 years), the primary focus being the explanation of high glacial $\Delta^{14}C_{atm}$ levels, and (3) a new 50,000-year record of the ^{14}C production rate, as inferred by deconvolving the reconstructed histories of $\Delta^{14}C_{atm}$ and CO_2 with a prognostic carbon cycle model and considering the uncertainties associated with the glacial-interglacial ocean carbon cycle. In the following sections we first introduce the Bern3D earth system model of intermediate complexity and describe the carbon cycle scenarios for forcing it. We then use step changes in the ^{14}C production rate and in selected parameters of the ocean carbon cycle model to gain insight into the transient and equilibrium response of $\Delta^{14}C_{atm}$. After these sensitivity experiments we present the results of paleoclimate simulations forced by available reconstructions of past changes in ^{14}C production together with reconstructed and hypothetical carbon cycle changes accompanying glacial-interglacial climate cycles. Finally, we present results for a first attempt to reconstruct the glacial history of the ^{14}C production rate using the Bern3D model forced with reconstructed variations in $\Delta^{14}C_{atm}$ and CO_2 as well as a wide range of carbon cycle scenarios. We end with a comparison of three fundamentally different (model-based, paleointensity-based, and ice-core ^{10}Be-based) reconstructions of atmospheric ^{14}C production.

2 Materials and methods

2.1 Brief description of the Bern3D model

147   Simulations are performed with the computationally efficient Bern3D earth system model of intermediate complexity

148   (version 2.0), which is designed for long-term climate simulations over several tens of thousands of years. The Bern3D

149   couples a frictional geostrophic 3-D ocean general circulation model (Edwards et al., 1998; Edwards and Marsh, 2005;

150   Müller et al., 2006), a 2-D energy-moisture balance atmosphere model (Ritz et al., 2011), an ocean carbon cycle model

151   (Müller et al., 2008; Tschumi et al., 2008; Parekh et al., 2008), a chemically active 10-layer ocean sediment model

152   (Heinze et al., 1999; Tschumi et al., 2011; Roth et al., 2014; Jeltsch-Thömmes et al., 2019), and a four-box model

153   representing carbon stocks in the terrestrial biosphere (Siegenthaler and Oeschger, 1987). The coarse-resolution ocean

154   model is implemented on a 41 x 40 horizontal grid, with 32 logarithmically spaced layers in the vertical. The seasonal

155   cycle is resolved with 96 time steps per year. The tracers carried in the ocean model include temperature, salinity,

156   dissolved inorganic carbon (DIC), dissolved organic carbon (DOC), carbon isotopes (^{14}C and ^{13}C) of DIC and DOC,

157   alkalinity (Alk), phosphate, silicate, iron, dissolved oxygen (O_2), preformed dissolved oxygen ($O_{2,pre}$), and an "ideal

158   age" tracer. The ideal age is set to zero in the surface layer, increased by Δt in all interior grid cells at each time step

159   of duration Δt, and transported by advection, diffusion, and convection. Atmospheric CO_2, $^{14}CO_2$, and $^{13}CO_2$ are also

160   carried as tracers in the atmosphere model. For a more complete description of the Bern3D model, the reader is referred

161   to Appendix A.

162

163   **2.2 Implementation of the ^{14}C tracer**

164

165   Natural radiocarbon (^{14}C) is a cosmogenic radionuclide produced in the atmosphere by cosmic radiation. Once

166   oxidized to $^{14}CO_2$, it participates in the global carbon cycle. Atmospheric $^{14}CO_2$ invades the ocean by air-sea gas

167   exchange, where it is subject to the same physical and biogeochemical processes that affect DIC. The only difference

168   is that ^{14}C is lost by radioactive decay (half-life of 5700 ± 30 years; Audi et al., 2003; Bé et al., 2013). The governing

169   natural processes, namely, atmospheric ^{14}C production, air-sea gas exchange, physical transport and mixing in the

170   water column, biological production and export of particulate and dissolved matter from the surface ocean, particle

171   flux through the water column, particle deposition on the sea floor, remineralization and dissolution in the water

172   column and the sediment pore waters, and vertical sediment advection and sediment accumulation, are explicitly

173   represented in the Bern3D model (see Fig. 2). Air-sea gas exchange is parameterized using a modified version of the

174   standard gas transfer formulation of OCMIP-2, with exchange rates that vary across time and space (see Appendix A

175   for more details).

176

177   Radiocarbon measurements are generally reported as Δ^{14}C, i.e., the ratio of ^{14}C to total carbon C relative to

178   that of the AD 1950 atmosphere, with a correction applied for fractionation effects, e.g., due to gas exchange and

179   photosynthesis (see Stuiver and Polach, 1977). In this model study, Δ^{14}C is treated as a diagnostic variable using the

180   two-tracer approach of OCMIP-2. Rather than treating the ^{14}C/C ratio as a single tracer, fractionation-corrected ^{14}C is

181   carried independently from the carbon tracer. The modelled ^{14}C concentration is normalized by the standard ratio of

182   the preindustrial atmosphere ($^{14}r_{std} = 1.170$ x 10^{-12}; Orr et al., 2017) in order to minimize the numerical error of

carrying very small numbers. For comparison to observations, $\Delta^{14}C$ is calculated from the normalized and fractionation-corrected modelled ^{14}C concentration as follows:

$$\Delta^{14}C = 1000\left(^{14}r' - 1\right) \tag{1}$$

where $^{14}r'$ is the ratio of $^{14}C/C$ in either atmospheric CO_2 or oceanic DIC divided by $^{14}r_{std}$, depending on the reservoir being considered. The approach taken to simulate atmospheric $^{14}CO_2$ is analogous to the approach used for CO_2, except that the equation includes the terms due to atmospheric production and radioactive decay. For simulations where the sediment model is active, the oceanic DIC tracer sees a constant input from terrestrial weathering, whereas there is no weathering input of $DI^{14}C$ to the ocean (see Appendix A for more details).

In the preindustrial spin-up simulation needed to initialize the Bern3D model, atmospheric CO_2 is held constant at 278.05 ppm and $\Delta^{14}C_{atm}$ at 0 permil. During this integration time the ocean inventories of carbon and ^{14}C adjust to the forcing fields. The resulting changes after >50,000 years of integration are negligibly small. Fig. 3 shows the steady-state $\Delta^{14}C$ distribution in the surface (< 100 m) and deep (> 1500 m) ocean for the preindustrial control run. The large-scale distribution of modelled oceanic $\Delta^{14}C$ broadly resembles the observed pattern in the Global Ocean Data Analysis Project (GLODAP; Key et al., 2004). That final state (i.e., the end of the preindustrial spin-up) is used to diagnose the ^{14}C production rate for the preindustrial atmosphere, such that the rate of ^{14}C production is balanced by radioactive decay and the net fluxes out of the atmosphere. For transient simulations, an adjustable scale factor is applied to the preindustrial steady-state value of 443.9 mol ^{14}C per year (1.66 atoms cm^{-2} s^{-1}) in order to account for production changes induced by solar and/or geomagnetic modulation. These production changes are derived from, e.g., available reconstructions of the ^{14}C production rate in relative units, as detailed in Sect. 2.5. Note the preindustrial spin-up results in steady-state values for weathering-derived inputs of DIC, Alk, P, and Si of 0.46 Gt C per year, 34.37 Tmol HCO_3^- per year, 0.17 Tmol P per year, and 6.67 Tmol Si per year, respectively. These terrestrial weathering rates were chosen to balance the sedimentation rates on the sea floor and are held fixed and constant throughout the simulations.

2.3 Model configurations

We focus in this paper on the response of $\Delta^{14}C_{atm}$ to changes in ^{14}C production and the ocean carbon cycle. For a deeper mechanistic understanding of the driving processes, step response experiments are first performed (see Sect. 3.1). These simulations include perturbations of the steady-state $^{14}C/C$ distribution under preindustrial conditions. We investigate the impact of step changes in (1) the ^{14}C production rate ("higher production" scenario), (2) wind stress and vertical diffusivity ("reduced deep ocean ventilation" scenario), and (3) the gas transfer velocity ("enhanced permanent sea ice cover" scenario). After a step change at time 0, the simulations are run to near-equilibrium over a 50,000-year integration. The following model configurations and therefore exchanging carbon reservoirs are

219 considered: atmosphere–ocean (OCN), atmosphere–ocean–land (OCN-LND), atmosphere–ocean–sediment (OCN-
220 SED), and atmosphere–ocean–land–sediment (ALL).

222 Next we examine the influence of changes that are transient in nature. We simulate $\Delta^{14}C_{atm}$ over the full range
223 of the ^{14}C dating method (i.e., 50 to 0 kyr BP) (see Sect. 3.2 and 3.3). These transient simulations are initialized at 70
224 kyr BP using model configuration ALL, and forced by reconstructed changes in ^{14}C production (see Sect. 2.5) over a
225 70,000-year integration. The first 20,000 years of the integration are considered a spin-up. Although the full record is
226 simulated, we focus our analysis on the millennial-scale variation in $\Delta^{14}C_{atm}$ before incipient deglaciation at ~18 kyr
227 BP. Eight model runs are carried out for each production rate reconstruction, using different combinations of forcing
228 fields and parameter values as described next.

230 **2.4 Carbon cycle scenarios**

232 In our transient simulations with the Bern3D model, eight scenarios based on different assumptions about the global
233 carbon cycle are considered, the details of which are summarized in Table 1. The goal is to investigate the extent to
234 which changes in the ocean carbon cycle could explain high glacial $\Delta^{14}C_{atm}$ levels, given available reconstructions of
235 past changes in ^{14}C production. We therefore consider a wide range of carbon cycle scenarios, including some extreme
236 cases. A note of caution. Because millennial-scale $\Delta^{14}C_{atm}$ variations during the last glacial are what we are interested
237 in, we do not attempt to reproduce abrupt climate perturbations such as Dansgaard-Oeschger warming events in the
238 model runs.

240 In the first scenario (MOD), the model is run with fixed preindustrial boundary conditions for the Earth's
241 orbital parameters, radiative forcing due to well-mixed greenhouse gases, and ice sheet extent. As a consequence,
242 atmospheric CO_2 remains approximately constant at the preindustrial level of 278.05 ppm over the simulation. The
243 second scenario (PAL) considers reasonably well-known climate forcing over the last glacial-interglacial cycle.
244 Simulations under this scenario are initialized with output from a previous spin-up simulation forced by glacial
245 boundary conditions with respect to orbital parameters (Berger, 1978), greenhouse gas radiative forcing based on
246 reconstructed atmospheric greenhouse gases (Köhler et al., 2017; Enting, 1987), and ice sheet extent. In simulations
247 under PAL, the model is integrated until 0 kyr BP following the reconstructed histories of the former. Ice sheets for
248 the preindustrial and Last Glacial Maximum (LGM) states are taken from Peltier (1994) and linearly scaled using the
249 global benthic $\delta^{18}O$ stack of Lisiecki and Stern (2016), which is a global ice volume proxy. Changes in the albedo,
250 salinity and latent heat flux associated with the ice sheet buildup or melting are also taken into account (Ritz et al.,
251 2011). Note that, although the radiative forcing for CO_2 is prescribed, the atmospheric CO_2 concentration is allowed
252 to evolve freely, except in the simulations described in Sect. 2.5.

254 Model scenario PAL appears to still be missing an important process or feedback for atmospheric CO_2, as it
255 cannot reproduce the observed low glacial CO_2 level without invoking additional changes (see, e.g., Tschumi et al.,

256 2011; Menviel et al., 2012; Roth and Joos, 2013; Jeltsch-Thömmes et al., 2019). Variations in atmospheric CO_2 govern

257 how fast $\Delta^{14}C$ signatures are passed between the atmosphere and ocean. Gross fluxes of ^{14}C between the atmosphere

258 and ocean, and vice versa, scale with atmospheric pCO_2 and its $^{14}C/C$ ratio. It is therefore important to reproduce low

259 glacial atmospheric CO_2 concentrations in at least some of the model scenarios, thereby capturing the influence of

260 temporal changes in CO_2 on the air-sea exchange of ^{14}C. In this study, we consider six scenarios that invoke additional

261 changes to force the model toward the observed low glacial CO_2 concentration. In addition to the PAL forcing, a time-

262 varying scale factor $F(t)$ is applied to some combination of tunable model parameters: wind stress scale factor τ,

263 vertical diffusivity K_V, gas transfer velocity k_w, $CaCO_3$-to-particulate organic carbon (POC) export ratio rr, and POC

264 remineralization length scale ℓ_{POC}. For the preindustrial period, the value of $F(t)$ is fixed at 1, whereas the theoretical

265 LGM value was chosen in order to achieve an atmospheric CO_2 concentration close to the LGM level of ~190 ppm

266 (see Table 1), as determined by sensitivity experiments. Note that the same values of $F(t)$ apply to any of the model

267 parameters considered in a given scenario. To obtain intermediate values, $F(t)$ is linearly scaled using the global

268 benthic $\delta^{18}O$ stack (see Fig. 1). For the spin-up needed to initialize these simulations, the glacial spin-up simulation

269 of PAL was integrated for 50,000 model years, with tunable parameters adjusted to their appropriate glacial values.

270 Atmospheric CO_2 drawdown of up to ~100 ppm is achieved over this 50,000-year integration. From that final spun-

271 up state, the model is run forward in time until 0 kyr BP with PAL and $F(t)$ forcing.

272

273   The first of these scenarios (CIRC) allows us to test the sensitivity of the model results with respect to changes

274 in ocean circulation. Tunable model parameters τ and K_V were reduced to 40 percent of their preindustrial values

275 throughout the global ocean during the LGM (i.e., $F_{\tau,K_V} = 0.4$). Such a drastic change in the wind stress field is not

276 realistic. Rather, these changes should be viewed as "tuning knobs" that force the ocean model into a poorly ventilated

277 state with an "older" ideal age and ^{14}C-depleted deep waters, as suggested for the glacial ocean (e.g., Sarnthein et al.,

278 2013; Skinner et al., 2017). In the model's implementation, a change in wind stress does not affect the gas transfer

279 velocity k_w, unlike in the real ocean where changes in wind stress and wind speed act together. The influence of a

280 change in air-sea exchange efficiency on the model results was investigated in a second scenario (VENT) where k_w

281 is reduced in the model's north (> 60°N) and south (> 48°S) polar areas in addition to global reductions of τ and K_V

282 ($F_{\tau,K_V,k_w} = 0.4$). A 60 percent reduction of k_w is unlikely to be correct but is a straightforward way to reduce the

283 model's gas exchange efficiency. In the third scenario (VENTx), reduction of polar k_w to 0 percent of its preindustrial

284 value was tested ($F_{\tau,K_V} = 0.4$; $F_{k_w} = 0.0$). Here, k_w remains fixed at 0 percent during the last glacial and is adjusted

285 to its preindustrial value via a linear ramp across the last glacial termination (~18 to 11 kyr BP). In this scenario, sea

286 ice would permanently cover 100 percent of the Southern Ocean during the last glacial, which is not supported by the

287 sea ice reconstructions of Gersonde et al. (2005) and Allen et al. (2011), and also the high-latitude (> 60°N) North

288 Atlantic and Arctic Ocean, for which there is some evidence (Müller and Stein, 2014; Hoff et al., 2016).

289

290   We end by investigating the sensitivity of the model results to changes in the parameters controlling the

291 export production of $CaCO_3$ and the water column remineralization of POC. Model scenario BIO considers changes

292 of the $CaCO_3$-to-POC export ratio (and thus also the $CaCO_3$-to-POC rain ratio; Archer and Maier-Reimer, 1994)

293   ($F_{rr} = 0.8$) and POC remineralization length scale (Roth et al., 2014) ($F_{\ell_{POC}} = 1.2$). These changes impact the global

294   carbon cycle by influencing the vertical gradients of DIC, Alk, and nutrients in the water column. A change in the

295   fluxes of POC and $CaCO_3$ to the sea floor drives a change in the magnitude of their removal by sedimentation on the

296   sea floor. A modest reduction in the export ratio during the last glacial is compatible with reconstructed variations in

297   carbonate ion concentrations (Jeltsch-Thömmes et al., 2019). How the depth of POC remineralization changed over

298   time is still unknown. The last two scenarios consider the combined effect of physical and biogeochemical changes:

299   PHYS-BIO ($F_{\tau,K_V,k_w,rr} = 0.7$) and PHYS-BIOx ($F_{\tau,K_V,k_w,rr} = 0.8$; $F_{\ell_{POC}} = 1.2$).

300

301   **2.5 Measurement- and model-based reconstruction of ^{14}C production**

302

303   Our ability to attribute past changes in $\Delta^{14}C_{atm}$ to climate-related changes in the ocean carbon cycle is limited by our

304   ability to reconstruct a precise and accurate history of the ^{14}C production rate. Past changes in ^{14}C production can be

305   estimated from geomagnetic field reconstructions and from [10]Be measurements in polar ice cores. For ice-core [10]Be-

306   based estimates, we use the ice-core radionuclide stack of Adolphi et al. (2018), which is based on [36]Cl data from the

307   GRIP ice core (Baumgartner et al., 1998), and on [10]Be data from the GRIP (Yiou et al., 1997; Baumgartner et al.,

308   1997; Wagner et al., 2001; Muscheler et al., 2004; Adolphi et al., 2014) and GISP2 (Finkel and Nishiizumi, 1997) ice

309   cores. It also includes [10]Be data from the NGRIP, EDML, EDC, and Vostok ice cores around the Laschamp

310   geomagnetic excursion (Raisbeck et al., 2017). It has been extended to the present using the [10]Be stack of Muscheler

311   et al. (2016). All ice cores were first placed on the same time scale (GICC05) before [10]Be fluxes were calculated. This

312   70,000-year [10]Be stack provides relative changes of ^{14}C production rates under the assumption that ^{14}C and [10]Be

313   production rates are directly proportional, as indicated by the most recent production rate models (e.g., Herbst et al.,

314   2017).

315

316   For paleointensity-based estimates, we employ (1) the North Atlantic Paleointensity Stack, or NAPIS, by Laj

317   et al. (2000) as extended by Laj et al. (2002), (2) the Global Paleointensity Stack, or GLOPIS, by Laj et al. (2004), (3)

318   a high-resolution paleointensity stack from the Black Sea (Nowaczyk et al., 2013), and (4) a paleointensity stack from

319   Iberian Margin sediments (Channell et al., 2018). In principle, stacks of widely distributed cores (NAPIS/GLOPIS)

320   are expected to yield a better representation of the global geomagnetic dipole moment, whereas the paleointensity

321   stacks from the Black Sea and the Iberian Margin avoid some of the problems associated with coring disturbances.

322   The four different paleointensity stacks were converted to ^{14}C production rates using the production rate model of

323   Herbst et al. (2017), the local interstellar spectrum of Potgieter et al. (2014), and assuming a constant solar modulation

324   potential of 630 MeV.

325

326   An alternative approach to estimating the ^{14}C production rate is to combine an atmospheric radiocarbon

327   budget with a prognostic carbon cycle model. Here simulations are performed with the Bern3D model and forced by

328   reconstructed changes in $\Delta^{14}C_{atm}$ and CO_2, as well as reconstructed and hypothetical carbon cycle changes, over the

329   last 50 kyr. Both the IntCal13 calibration curve (Reimer et al., 2013) and the recent Hulu Cave $\Delta^{14}C_{atm}$ dataset (Cheng

330   et al., 2018) are used. Note that although the forthcoming IntCal20 calibration curve (Reimer et al., in press) will be
331   the new standard atmospheric radiocarbon record for the last 55,000 years, essentially all data underlying IntCal20
332   before 13.9 kyr BP are tied to the Hulu Cave dataset, either via time scales (Lake Suigetsu plant macrofossil data) or
333   marine reservoir corrections (marine records). Hence, the IntCal20 and Hulu Cave $\Delta^{14}C_{atm}$ records are very similar
334   and using IntCal20 would not impact our conclusions.
335
336   The ^{14}C production rate Q is calculated, each model year, from the air-sea $^{14}CO_2$ flux (F_{as}), the atmosphere-
337   land $^{14}CO_2$ flux (F_{ab}), the loss of ^{14}C due to radioactive decay, and the change ($\dot{I}_a$) in the atmospheric ^{14}C inventory
338   (I_a):
339
340    $Q = F_{as} + F_{ab} + \lambda I_a + \dot{I}_a$ (2)
341
342   where λ is the radioactive decay constant for ^{14}C, i.e., $\lambda = \ln 2 / 5700$ years $= 1.2160$ x 10^{-4} yr^{-1}. The radioactive decay
343   term λI_a and the change in inventory $\dot{I}_a$ follow the reconstructed $\Delta^{14}C_{atm}$ and CO_2 records, whereas F_{as} and F_{ab} are
344   explicitly computed by the model. The F_{as} term depends strongly on the carbon cycle scenario under consideration
345   (see Sect. 2.4 and Table 1). For comparison with other reconstructions, Q is converted into a relative value by
346   normalizing it by the preindustrial value.
347
348   **3 Results and discussion**
349
350   **3.1 Atmospheric $\Delta^{14}C$ response to step changes**
351
352   We use step changes in the ^{14}C production rate, and in selected carbon cycle parameters, to gain insight into the
353   characteristic magnitude and time scale of the corresponding $\Delta^{14}C_{atm}$ changes (Fig. 4). Besides variations of the
354   production rate, changes in ocean circulation and air-sea gas exchange are considered the most important factors
355   affecting $\Delta^{14}C_{atm}$. Their effect on $\Delta^{14}C_{atm}$ can be understood in terms of their effect on the reservoir sizes involved in
356   the global carbon cycle and on the exchange rates between the reservoirs. We investigate the relative importance of
357   the major global carbon reservoirs (atmosphere, terrestrial biosphere, ocean, and sediments) by considering four
358   different model configurations (see Sect. 2.3), with particular emphasis on the role of marine sediments.
359
360   In model studies, the process of sedimentation (defined here as the difference between deposition and
361   remineralization/dissolution of material on the sea floor) is often neglected because it is a relatively minor flux. In the
362   Bern3D model, sedimentation removes only about 0.46 Gt C and 45.31 mol ^{14}C per year in the preindustrial steady
363   state. Indeed, the interaction with the ocean sediments has little influence on the global mean value of oceanic $\Delta^{14}C$
364   and therefore $\Delta^{14}C_{atm}$, as long as the total oceanic amount of carbon remains approximately constant (Siegenthaler et
365   al., 1980); however, this is not always true, particularly in the case of millennial-scale climate perturbations. This is
366   demonstrated by the differences between the model runs with and without sediments (i.e., ALL versus OCN-LND,

10

367 and OCN-SED versus OCN) as shown in Fig. 4. The response of $\Delta^{14}C_{atm}$ to various perturbations depends on the
368 magnitude of the change in the ocean carbon inventory, with a larger change achieved by considering the interaction
369 with the ocean sediments and the imbalance between weathering and sedimentation (see Fig. 5e,f). In order to facilitate
370 our discussion, we will make only direct comparisons between model runs ALL and OCN-LND, which both include
371 the four-box terrestrial biosphere model. We note that the ^{14}C exchange rate between the atmosphere and the terrestrial
372 biosphere is only of minor importance for long time scales of millennia and more.

373

374 **3.1.1 Change of ^{14}C production**

375

376 At steady state, the relative change of $\Delta^{14}C_{atm}$ is equal to the relative change of the ^{14}C production rate, irrespective of
377 the individual reservoirs considered. Fig. 4 shows that $\Delta^{14}C_{atm}$ increases by about 100 permil (or 10 percent) when the
378 production rate is increased by 10 percent. In model run ALL, $\Delta^{14}C_{atm}$ increases approximately exponentially to its
379 new steady-state value with a characteristic time constant T of about 6170 years (i.e., $1 - 1/e \approx 63$ percent of the
380 total change in $\Delta^{14}C_{atm}$ occurs within 6170 years). This e-folding time scale is close to the mean lifetime of ^{14}C (~8223
381 years), which is modulated by the time required for $\Delta^{14}C$ to equilibrate between the atmosphere and the ocean (i.e.,
382 the time scale for deep ocean ventilation, of the order of hundreds of years to 1000 years or more). In the next section,
383 we will investigate the effect of ocean carbon cycle processes on $\Delta^{14}C_{atm}$.

384

385 Note that for simplicity, we investigated only step changes in atmospheric production, although, in reality,
386 ^{14}C production varies continuously over time due to changes in the solar and/or geomagnetic modulation of the cosmic
387 radiation. This results in a non-steady state value of $\Delta^{14}C_{atm}$.

388

389 **3.1.2 Change of ocean circulation**

390

391 The exchange rate between the surface and deep ocean is mainly determined by physical transport and mixing
392 processes. The overall effect of these processes is to transport ^{14}C-enriched surface waters to the thermocline and deep
393 ocean, where waters are typically ^{14}C-depleted. In addition, the nutrient supply by transport and mixing plays an
394 important role in determining the production and export of biogenic material from the surface ocean, constituting a
395 second pathway for transporting ^{14}C to the deep ocean.

396

397 In the Bern3D model, the tunable model parameters affecting the ventilation of the deep ocean include a
398 scale factor τ for the wind stress field and vertical diffusivity K_V. Fig. 4 shows the $\Delta^{14}C_{atm}$ response after a sudden
399 decrease of τ and K_V by 50 percent. Although a halving of τ and K_V does not represent a realistic change, the resulting
400 state of the ocean's large-scale overturning circulation can be interpreted in terms of the "ideal age" of water, which
401 represents the average time since a water mass last made surface boundary contact. The new steady-state ideal age
402 after a halving of τ and K_V is almost three times greater than the preindustrial steady-state value (i.e., ~1664 years
403 versus ~613 years). This "ageing" of the ocean is achieved through a weakening and shoaling of the global meridional

404   overturning circulation as evident from a moderate reduction in the meridional overturning stream function for the
405   Indo-Pacific Ocean from about 14 to 9.5 Sv (1 Sv = 10^6 m^3 s^{-1}), and a very strong reduction from about 18 to 8 Sv in
406   the Atlantic meridional overturning stream function, consistent with evidence for the glacial ocean. Here, as expected,
407   the overall effect of deep water ageing is a stronger vertical Δ^{14}C gradient in the water column and a subsequent
408   increase in Δ^{14}C$_{atm}$. The exact nature of the Δ^{14}C$_{atm}$ response, however, depends on the carbon reservoirs considered.
409
410   If the ocean sediment reservoir is neglected, the time required for Δ^{14}C$_{atm}$ to adjust to step changes in τ and
411   K_V is relatively short. Δ^{14}C$_{atm}$ increases rapidly to its new steady-state value of ~159 permil, with a time constant T of
412   about 600 years. This increase of Δ^{14}C$_{atm}$ can be explained by the fact that, owing to a weaker and shallower
413   overturning circulation, a comparatively large amount of carbon is moved from the atmosphere to the ocean. More
414   specifically, the atmospheric carbon inventory decreases by 14.6 percent, whereas the atmospheric ^{14}C inventory
415   decreases by only 1.1 percent (Fig. 5c). The ^{14}C being produced in the atmosphere is therefore diluted by a smaller
416   carbon inventory, increasing the atmospheric ^{14}C/C ratio; this asymmetry in the drawdown of CO$_2$ and ^{14}CO$_2$ is what
417   permits the increase of Δ^{14}C$_{atm}$. Since the ocean carbon inventory changes by only +0.2 percent, the mean Δ^{14}C value
418   for the global ocean is nearly unaffected, a decrease of only ~11 permil in the new steady state (Fig. 6g).
419
420   In the model run where the sediment model is active, there are two distinct time constants. A rapid increase
421   of Δ^{14}C$_{atm}$ occurs, ~143 permil in the first few hundred years, then Δ^{14}C$_{atm}$ gradually decreases to its final value of ~91
422   permil after tens of thousands of years. Reduced deep ocean ventilation is again responsible for the rapid Δ^{14}C$_{atm}$
423   change and the respective time constant (T = ~480 years). The second time constant of ~23,390 years is due to the
424   relatively long time required for the ocean carbon inventory to adjust to the ocean circulation-driven imbalance
425   between weathering and sedimentation.
426
427   The process of ocean circulation interacts with the efficiency of the ocean's biological carbon pump, via its
428   impact on export production, ocean interior oxygen levels, and seawater carbonate chemistry/equilibria. This has
429   important implications for the sedimentation of biogenic material on the sea floor and, on a time scale of tens of
430   thousands of years, the total oceanic amount of carbon. Through this coupling of ocean circulation and sea floor
431   sedimentation via the biological carbon pump, a halving of τ and K_V leads to a 9.8 percent increase of the ocean carbon
432   inventory in the new steady state (Fig. 5e). Qualitatively, a reduction in the ocean's overturning circulation leads to a
433   lower surface nutrient supply, which limits the production and export of biogenic material from the surface ocean.
434   This, in turn, decreases the fluxes of POC and CaCO$_3$ to the sea floor, with major consequences for the magnitude of
435   their removal by sedimentation. At the same time, a constant input of DIC, Alk, and nutrients is added to the ocean
436   from terrestrial weathering which is no longer balanced by sedimentation on the sea floor (this is what permits a larger
437   ocean carbon inventory). The overall effect is a gradual reduction of oceanic Δ^{14}C by ~76 permil (Fig. 6g), which
438   dilutes the initial Δ^{14}C$_{atm}$ peak by 52 permil.
439
440   **3.1.3 Change of gas transfer velocity**

441

442 It takes about a decade for the isotopic ratios of carbon to equilibrate between the atmosphere and a ~75-m thick

443 surface mixed layer by air-sea gas exchange (Broecker and Peng, 1974). A consequence of this is that the surface

444 ocean is undersaturated with respect to $\Delta^{14}C_{atm}$ (see Fig. 3). The choice of gas transfer velocity k_w as a function of

445 wind speed is critical for the efficiency of air-sea gas exchange. A reduction of k_w corresponds to a higher resistance

446 for gas transfer across the air-sea interface, which means that the ^{14}C produced in the atmosphere escapes into the

447 surface ocean at a slower rate. The effect of a lower k_w is a larger air-sea gradient of $\Delta^{14}C$ and higher $\Delta^{14}C_{atm}$ values.

448 In contrast, the $\Delta^{14}C$ value for the surface ocean is nearly unaffected so long as the ocean carbon inventory remains

449 approximately constant, since the vertical gradient of $\Delta^{14}C$ in the ocean is dominated by physical transport and mixing

450 processes. Although the exact nature of the gas transfer velocity under glacial climate conditions remains unclear, k_w

451 represents a straightforward way to reduce the model's air-sea exchange efficiency due to theoretical changes in wind

452 stress, sea ice, etc.

453

454 Fig. 4 shows how $\Delta^{14}C_{atm}$ responds to a perturbation in the gas transfer velocity. In the model run without

455 sediments, reduction of k_w to 0 percent of its preindustrial value, in the model's north (> 60°N) and south (> 48°S)

456 polar areas, leads to a moderate increase of $\Delta^{14}C_{atm}$ in the new steady state. The amplitude of $\Delta^{14}C_{atm}$ change is ~42

457 permil, which is achieved with an e-folding time scale T of about 180 years. This relatively short time constant can be

458 explained by the multidecadal time scale required for $\Delta^{14}C$ to equilibrate between the model's atmosphere, upper

459 ocean, and terrestrial biosphere. As shown in Fig. 6, the mean $\Delta^{14}C$ values for the surface, deep, and global ocean in

460 the new steady state are only slightly different from the preindustrial steady-state values, as expected from the fact

461 that the ocean carbon inventory remains relatively stable.

462

463 Interestingly, if sediments are included in the model, the final value of $\Delta^{14}C_{atm}$ is much higher (~91 permil).

464 In this case, a perturbation in k_w leads to a very rapid initial increase of $\Delta^{14}C_{atm}$ (~42 permil), and a much slower

465 subsequent increase of $\Delta^{14}C_{atm}$ (~49 permil). The latter has an e-folding time scale T of about 14,200 years. This slow

466 doubling of the initial $\Delta^{14}C_{atm}$ increase is unexpected, but can be explained by the fact that a reduction of k_w involves

467 also a reduction of air-sea O_2 gas exchange in the deep water formation regions, decreasing the oceanic oxygen that

468 is available for transport to the deep ocean. This, in turn, implies lower oxygen concentrations in the water column

469 and the sediment pore waters, decreasing the rate of POC remineralization in the sediments. Reducing this has the

470 overall effect of enhancing POC sedimentation on the sea floor, causing the ocean carbon inventory to decrease. As

471 shown in Fig. 5f, the total oceanic amount of carbon decreases by 5.9 percent in the new steady state, resulting in

472 elevated $\Delta^{14}C$ values for the surface (+56 permil), deep (+30 permil), and global (+37 permil) ocean as well as for the

473 atmosphere (+91 permil) (see Fig. 6). Note that the increase in $\Delta^{14}C_{atm}$ is not accompanied by a significant change in

474 the atmospheric carbon inventory, which decreases by only 2.2 to 3.3 percent. The air-sea equilibration time scale for

475 CO_2 by gas exchange is about 1 year for a ~75-m thick surface mixed layer (Broecker and Peng, 1974), which is much

476 smaller than the ventilation time scale for the deep ocean (on the order of several hundred years or more). One would

477 therefore expect that the oceanic uptake of CO_2 demonstrates only a very small response to changes in k_w.

478

479   Overall, findings from these sensitivity experiments demonstrate that (1) the response of $\Delta^{14}C_{atm}$ to changes

480   in the internal parameters of the ocean carbon cycle, in contrast to ^{14}C production changes, depends strongly on

481   whether or not the balance between terrestrial weathering and sedimentation on the sea floor is simulated, (2) the e-

482   folding time scale for the initial adjustment of $\Delta^{14}C_{atm}$ to ocean carbon cycle changes, i.e., changes in ocean circulation

483   and gas exchange, is shorter than that for production changes (i.e., ~600 years and ~180 years versus ~6170 years),

484   (3) air-sea gas exchange, in contrast to ocean circulation, has only a small effect on atmospheric CO_2, given that gas

485   exchange is not the rate-limiting step for oceanic CO_2 uptake, and (4) on time scales of tens of thousands of years

486   changes in the balance between weathering and sedimentation can potentially diminish (or elevate) the $\Delta^{14}C_{atm}$ value.

487   This is new, important information for future paleoclimate simulations and suggests that changes in $\Delta^{14}C_{atm}$ may be

488   overestimated (or underestimated) in models that do not simulate the interaction between sea floor sediments and the

489   overlying water column.

490

491   **3.2 Role of ^{14}C production in past atmospheric $\Delta^{14}C$ variability**

492

493   We now consider the component of past $\Delta^{14}C_{atm}$ variability caused by production changes alone. Fig. 7 shows the

494   results of model runs using different reconstructions of the ^{14}C production rate, as inferred from paleointensity data

495   and from ice-core ^{10}Be fluxes. The global carbon cycle is assumed to be constant and under preindustrial conditions

496   for these simulations (i.e., scenario MOD is used). Our analysis is restricted to the glacial portion of the record (50 to

497   18 kyr BP), in part because this is the time period which experiences the largest production changes, and in part

498   because we did not attempt to reproduce the ~80 ppm change in atmospheric CO_2 that occurred during the last glacial

499   termination. As we have already noted, much research over the last decades has attempted to explain the observed

500   glacial-interglacial variations in $\Delta^{14}C_{atm}$ and CO_2, and this was not the goal of this study.

501

502   At first glance, the millennial-scale structure of model-simulated $\Delta^{14}C_{atm}$ is comparable to that of the

503   reconstructions. These similarities appear to be highest for the oldest portion of the record, roughly before 30 kyr BP.

504   The model reproduces major features of the reconstructed $\Delta^{14}C_{atm}$ variability such as the large changes associated with

505   the Laschamp (~41 kyr BP) and Mono Lake (~34 kyr BP) geomagnetic excursions. These two events are clearly

506   expressed as distinct maxima in all model-simulated records. A more detailed comparison reveals a high correlation

507   between the modelled and reconstructed $\Delta^{14}C_{atm}$ values between 50 and 33 kyr BP. Of note is the better agreement

508   with the new Hulu Cave $\Delta^{14}C_{atm}$ dataset as compared to the IntCal13 calibration curve (i.e., Pearson correlation

509   coefficient r of 0.96 versus 0.91). This is likely due to the fact that the Laschamp excursion is smoothed/smeared out

510   during the stacking process of the IntCal13 $\Delta^{14}C_{atm}$ datasets (Adolphi et al., 2018). The correlation between modelled

511   and reconstructed $\Delta^{14}C_{atm}$ is much weaker during the millennia after the Mono Lake excursion (33 to 18 kyr BP; r =

512   0.52 to 0.64). While it is clear that much of the millennial-scale variation in $\Delta^{14}C_{atm}$ is driven by past changes in ^{14}C

513   production, the model fails to reproduce the glacial level of $\Delta^{14}C_{atm}$ and also does not capture the ~15,000-year

514   persistent elevation of $\Delta^{14}C_{atm}$ or the subsequent decrease of $\Delta^{14}C_{atm}$ after ~25 kyr BP.

515

516   The reconstructions suggest that the highest values of $\Delta^{14}C_{atm}$ occurred during the Laschamp excursion, with

517 a maximum value of ~595 permil at 41.1 kyr BP found in the IntCal13 record. The Hulu Cave record indicates even

518 higher values for the Laschamp event $\Delta^{14}C_{atm} = $ ~742 permil, at 39.7 kyr BP). In contrast, the model is able to simulate

519 maximum $\Delta^{14}C_{atm}$ values of only ~364 permil at 40.4 kyr BP, and ~236 permil at 40.5 kyr BP, as predicted by the

520 paleointensity-based and ice-core ^{10}Be-based production rate estimates, respectively. Although the model is unable to

521 reproduce the reconstructed values of $\Delta^{14}C_{atm}$, the modelled amplitude of the variation in $\Delta^{14}C_{atm}$ in response to the

522 Laschamp event shows a reasonable agreement with the reconstructed amplitude of $\Delta^{14}C_{atm}$ change found in the

523 IntCal13 record (~240 permil). The $\Delta^{14}C_{atm}$ change predicted by paleointensity data has a maximal amplitude of about

524 320 permil, whereas the ice-core ^{10}Be data indicate a smaller amplitude (~224 permil). Note that the IntCal13 and

525 model-simulated amplitudes of the Laschamp-related $\Delta^{14}C_{atm}$ change are about two times smaller than that observed

526 in the Hulu Cave record (~575 permil), which is more likely to be correct.

527

528   Moving onto the full glacial record (50 to 18 kyr BP), there are considerable discrepancies between

529 reconstructed and modelled $\Delta^{14}C_{atm}$ ($\Delta\Delta^{14}C$; see Fig. 7). The use of ice-core ^{10}Be data to predict past changes in $\Delta^{14}C_{atm}$

530 results in the largest $\Delta\Delta^{14}C$, with offsets between the records as high as ~544 to 558 permil (root-mean-square error

531 *RMSE* = 404 to 408 permil). Model-simulated $\Delta^{14}C_{atm}$ given by paleointensity data varies widely between the four

532 available reconstructions, yielding $\Delta\Delta^{14}C$ values of ~325 to 639 permil (*RMSE* = 206 to 455 permil). Note that the

533 upper limit of the paleointensity-based $\Delta\Delta^{14}C$ overlaps with the ice-core ^{10}Be-based $\Delta\Delta^{14}C$. Given the uncertainties

534 associated with the reconstruction of past changes in ^{14}C production, accurate predictions of its contribution to past

535 changes in $\Delta^{14}C_{atm}$ are challenging. Nonetheless, the substantial systematic offsets between the reconstructed and

536 model-simulated $\Delta^{14}C_{atm}$ records after ~33 kyr BP point toward insufficiently high ^{14}C production rates over this period

537 of time. The question arises as to whether another factor besides geomagnetic modulation of the cosmic ray intensity

538 was responsible for elevated glacial $\Delta^{14}C_{atm}$ levels. The effect of ocean carbon cycle changes on the evolution of

539 $\Delta^{14}C_{atm}$ is considered next.

540

541 **3.3 Carbon cycle contribution to high glacial atmospheric $\Delta^{14}C$ levels**

542

543 Here we investigate the magnitude and timing of the maximum possible $\Delta^{14}C_{atm}$ change during the last glacial period,

544 obtained by running the Bern3D model with eight different carbon cycle scenarios (see Table 1). For the sake of

545 clarity, we will discuss only the results of model runs using the mean paleointensity-based ^{14}C production rate, though

546 all available reconstructions were used. We emphasize that this is not a best-guess estimate of paleointensity-based

547 ^{14}C production. One should focus on the relative changes of $\Delta^{14}C_{atm}$ between model scenarios, and how specific carbon

548 cycle processes affect the glacial level of $\Delta^{14}C_{atm}$.

549

550   Modelled 50,000-year records of $\Delta^{14}C_{atm}$ and CO_2 as well as their reconstructed histories are shown in Fig.

551 8. In order to provide a basis for comparison of modelling efforts, the results of model run MOD (which assumes a

552   constant preindustrial carbon cycle) are presented. The influence of ocean carbon cycle changes on $\Delta^{14}C_{atm}$ was tested

553   in the other model runs. Interestingly, the forcing fields for model run PAL (orbital parameters, greenhouse gas

554   radiative forcing, and ice sheet extent) have only a minimal impact on $\Delta^{14}C_{atm}$. The PAL forcing fields also do not

555   achieve sufficiently low glacial CO_2 concentrations. Only a slight reduction of atmospheric CO_2 by ~20 ppm could be

556   achieved, which unrealistically occurs during the last glacial termination (CO_2 = 258.07 ppm, at 14.6 kyr BP). With

557   hypothetical carbon cycle changes, the agreement between observed and modelled CO_2 during the last glacial period

558   is good (as by design), but the deglacial CO_2 rise is lagged and ~60 ppm too small at 11 kyr BP. Since this study

559   focuses on glacial $\Delta^{14}C_{atm}$ levels before incipient deglaciation at ~18 kyr BP, we will not discuss the lag any further.

560

561   Model simulation of high glacial $\Delta^{14}C_{atm}$ levels can be significantly improved by considering hypothetical

562   carbon cycle changes in conjunction with PAL forcing. The amplitude of $\Delta^{14}C_{atm}$ change is highest for runs CIRC,

563   VENT, and VENTx. This behavior is due to the fact that, owing to a reduction of τ, K_V, and k_w, strong vertical $\Delta^{14}C$

564   gradients in the ocean, as well as a large air-sea $\Delta^{14}C$ gradient, are established. As shown in Fig. 8, a more sluggish

565   ventilation of deep waters is clearly expressed as an increase in the model ocean's global average ideal age and surface-

566   and deep-water reservoir ages, where the latter two are calculated for the surface ocean and bottom water grid cells,

567   respectively. These are equivalent to radiocarbon reservoir age offsets following Soulet et al. (2016). The deep-water

568   reservoir age (i.e., B-Atm ^{14}C age offset, or B-Atm) provides a measure of the radiocarbon disequilibrium between

569   the deep ocean and the atmosphere, which arises due to the combined effect of air-sea gas exchange efficiency and

570   the deep ocean ventilation rate, whereas the effect of upper ocean stratification and/or sea ice on air-sea gas exchange

571   is particularly important for surface reservoir ages (i.e., surface R-age) (Skinner et al., 2019).

572

573   Driven by a reduction in ocean circulation, model run CIRC predicts a substantial increase in B-Atm during

574   the last glacial, which is defined here as 40 to 18 kyr BP to avoid biasing global mean estimates toward Laschamp

575   values. The global average glacial B-Atm predicted by CIRC is ~3225 ^{14}C years, representing an increase in B-Atm

576   of ~1599 ^{14}C years relative to the preindustrial value of ~1626 ^{14}C years. Model run VENT predicts a slightly larger

577   increase in glacial B-Atm due to the inhibition of air-sea gas exchange. The "oldest" glacial waters are found in model

578   run VENTx where air-sea gas exchange is severely restricted, yielding an increase in B-Atm of ~1912 ^{14}C years

579   (glacial B-Atm ~3538 ^{14}C years). The glacial B-Atm values given by runs CIRC, VENT, and VENTx, as well as the

580   ~717 year increase in ideal age during the last glacial relative to preindustrial, suggest that the glacial deep ocean was

581   about two times older than its preindustrial counterpart. Comparison of our LGM B-Atm estimates (range of 3682 to

582   3962 ^{14}C years) with the compiled LGM marine radiocarbon data of Skinner et al. (2017) demonstrate that the carbon

583   cycle scenarios are extreme, although it should be noted that Skinner et al. consider a wider depth range (~500 to 5000

584   m) of the ocean than we do. Skinner et al. (2017) predict a global average LGM B-Atm value of ~2048 ^{14}C years, an

585   increase of ~689 ^{14}C years relative to preindustrial. Turning our comparison to surface reservoir ages, we note that

586   our global average LGM surface R-age of ~1132 ^{14}C years from runs VENT and VENTx is comparable to the ~1241

587   ^{14}C years obtained by Skinner et al. (2017) for the LGM. The model-based estimates of surface R-age from Butzin et

588   al. (2017) indicate a much lower LGM value of ~780 ^{14}C years, and values ranging from 540 to 1250 ^{14}C years between

589   50 and 25 kyr BP. Note that these estimates are based on model-simulated values between 50°N and 50°S. If the polar

590   regions are included in the calculation (see Fig. 8c), their surface R-age estimates become comparable to our glacial

591   values (range of 911 to 1354 ^{14}C years), and between about 34 and 22 kyr BP can exceed them, including even those

592   from model runs VENT and VENTx, unless $\Delta^{14}C_{atm}$ and CO_2 are prescribed (dashed colored lines in Fig. 8c) as in the

593   simulation by Butzin et al. (2017).

594

595   Indirect evidence for deep water ageing can be provided by the occurrence of depleted ocean interior oxygen

596   levels, due to the progressive consumption of dissolved oxygen during organic matter remineralization in the water

597   column. This situation is amplified by the slow escape of accumulating remineralized carbon in the ocean interior

598   (see, e.g., Skinner et al., 2017), leading to higher values of apparent oxygen utilization ($AOU = O_{2,pre} - O_2$). These

599   two concepts (increased AOU and increased B-Atm) taken together signal a significant reduction in deep ocean

600   ventilation characterized by a decrease in the exchange rate between younger (higher $\Delta^{14}C$) surface waters and older

601   (^{14}C-depleted), carbon-rich deep waters. Model runs CIRC, VENT, and VENTx do indeed indicate a large increase in

602   AOU of about 95 mmol m^{-3} from its preindustrial value of ~150 mmol m^{-3}. The reason for this AOU increase is that

603   a reduction of deep ocean ventilation permits enhanced accumulation of remineralized carbon in the ocean interior

604   and therefore a more efficient biological carbon pump. Model runs BIO, PHYS-BIO, and PHYS-BIOx allow us to

605   investigate the impact of other biological carbon pump changes on $\Delta^{14}C_{atm}$ and CO_2 (i.e., changes in the CaCO$_3$-to-

606   POC export ratio and POC remineralization length scale). While these changes lead to an effective atmospheric CO_2

607   drawdown mechanism, model results confirm that their effect on $\Delta^{14}C_{atm}$ is much less important (see Fig. 8).

608

609   Model run VENTx gives the best results with respect to glacial levels of $\Delta^{14}C_{atm}$, with a maximum

610   underestimation of ~202 to 229 permil ($RMSE$ = 103 to 110 permil) and a relatively good correlation (r = 0.79 to

611   0.91). Only one model parameter was changed for run VENTx as compared to runs CIRC and VENT, namely, the

612   polar gas transfer velocity k_w was reduced to 0 percent of its preindustrial value during the last glacial. In this extreme

613   scenario, we assume that sea ice cover extended in the northern hemisphere as far south as 60°N and in the southern

614   hemisphere as far north as 48°S, which is not supported by the reconstructions (Gersonde et al., 2005; Allen et al.,

615   2011). Nonetheless, considering extreme assumptions about polar air-sea exchange efficiency under glacial climate

616   conditions is interesting for two reasons: (1) a change in gas exchange hardly affects the atmospheric CO_2

617   concentration, and (2) an additional change of $\Delta^{14}C_{atm}$ could possibly be achieved on a time scale of tens of thousands

618   of years by changing the balance between weathering and sedimentation (see Sect. 3.1.3). This behavior has important

619   implications for the glacial atmosphere, which is characterized by high $\Delta^{14}C$ levels in conjunction with low but

620   relatively stable CO_2 concentrations. In contrast to a change in ocean circulation, air-sea gas exchange is a dedicated

621   $\Delta^{14}C_{atm}$ "control knob" that can be invoked by models for a further increase of $\Delta^{14}C_{atm}$ without changing atmospheric

622   CO_2. Here, an additional increase in $\Delta^{14}C_{atm}$ of ~130 permil relative to CIRC and VENT is achieved if gas exchange

623   is reduced permanently to 0 percent in the polar regions.

624

625   While the modelled $\Delta^{14}C_{atm}$ values obtained by VENTx show rather good agreement with the reconstructions

626   between 50 and 33 kyr BP ($r = 0.92$ to 0.96; $RMSE = 74$ to 102 permil), considerable discrepancies remain for the

627   younger portion of the record. The analysis shown in Fig. 9 illustrates that even with extreme changes in the ocean

628   carbon cycle it is very difficult to reproduce the reconstructed $\Delta^{14}C_{atm}$ values after ~33 kyr BP. During this period of

629   time, VENTx underestimates $\Delta^{14}C_{atm}$ by up to ~203 permil ($RMSE = 118$ to 128 permil), and is very poorly ($r = 0.1$)

630   correlated with the reconstructions, confirming that there are still considerable gaps in our understanding. Although it

631   may be possible that permanent North Atlantic-Arctic and Antarctic sea ice cover extended to lower and higher

632   latitudes than previously reconstructed, we conclude from our model study that even extreme assumptions about sea

633   ice cover are insufficient to explain the elevated $\Delta^{14}C_{atm}$ levels after ~33 kyr BP. It appears instead that the glacial ^{14}C

634   production rate was higher than previously estimated and/or the reconstruction of glacial $\Delta^{14}C_{atm}$ levels is biased high.

635   The older portion of the $\Delta^{14}C_{atm}$ record is based on data from archives other than tree rings (i.e., plant macrofossils,

636   speleothems, corals, and foraminifera) (Reimer et al., 2013), providing, except for the Lake Suigetsu plant macrofossil

637   data (Bronk Ramsey et al., 2012), only indirect measurements of $\Delta^{14}C_{atm}$. Note that these data show uncertainty in

638   calendar age that propagate into the estimation of past $\Delta^{14}C_{atm}$ levels.

639

640   Large uncertainties in the pre-Holocene ^{14}C production rate also hamper our qualitative and quantitative

641   interpretation of the $\Delta^{14}C_{atm}$ record. There is considerable disagreement between the available reconstructions of past

642   changes in ^{14}C production (Fig. 1). Paleointensity-based estimates typically predict higher ^{14}C production rates than

643   ice-core ^{10}Be-based ones. An exception is the paleointensity stack from Channell et al. (2018), which predicts lower

644   production rates. But, irrespective of the scatter, it is clear that all of the ^{14}C production rate estimates are insufficiently

645   high to explain the elevated $\Delta^{14}C_{atm}$ levels during the last glacial. Given the uncertainties in these estimates, it is very

646   difficult to quantitatively describe the role of the ocean carbon cycle in determining the $\Delta^{14}C$ and CO_2 levels in the

647   glacial atmosphere.

648

649   **3.4 Reconstructing the ^{14}C production rate by deconvolving the atmospheric $\Delta^{14}C$ record**

650

651   The unresolved discrepancy between reconstructed and model-simulated $\Delta^{14}C_{atm}$ raises the question how the ^{14}C

652   production rate would have had to evolve to be consistent with the IntCal13 calibration curve or the new Hulu Cave

653    $\Delta^{14}C_{atm}$ dataset. This question is addressed by deconvolving the $\Delta^{14}C_{atm}$ reconstruction over the last 50 kyr, using the

654   Bern3D carbon cycle model forced with reconstructed histories of $\Delta^{14}C_{atm}$ and CO_2 (see Eq. [2]). The carbon cycle

655   scenarios described in Table 1, with the exception of MOD, are used in order to provide an estimate of the uncertainty

656   associated with the model's glacial ocean carbon cycle. We note that the carbon cycle scenarios are not designed to

657   capture the specific features of the last glacial termination, and therefore the results of the deconvolution over this

658   time period must be considered very preliminary (and regarded as tentative). A detailed analysis of the Holocene ^{14}C

659   production rate is available in the literature (Roth and Joos, 2013). Finally, we consider the uncertainties associated

660   with the older portion of the $\Delta^{14}C_{atm}$ record by deconvolving both the IntCal13 and Hulu Cave $\Delta^{14}C_{atm}$ records. Hulu

661   Cave data overlap with IntCal13 between ~10.6 and 33.3 kyr BP (Cheng et al., 2018), as expected from the fact that

662   IntCal13 between 10.6 and 26.8 kyr BP is based in part on Hulu Cave stalagmite H82 (Southon et al., 2012), whereas
663   there are substantial offsets before ~30 kyr BP.

664

665   Fig. 10 shows the new, model-based reconstruction of past changes in ^{14}C production compared with
666   available measurement-based reconstructions. Before the onset of the Laschamp excursion at ~42 kyr BP, production
667   rates as inferred from the Hulu Cave record are near modern levels, whereas those obtained from the IntCal13 record
668   are somewhat higher than modern. As expected, peak production occurs during the Laschamp event (~42 to 40 kyr
669   BP), with the Hulu Cave dataset yielding the largest amplitude (factor of ~2 greater than modern). The IntCal13 record
670   predicts a smaller amplitude of ~1.6 times the modern value. Both $\Delta^{14}C_{atm}$ records predict production minima at ~37
671   kyr BP (~7 percent higher than modern) and ~32 kyr BP (~5 percent higher than modern), interrupted by a prominent
672   peak (factors of ~1.5 and ~1.4, respectively) during the Mono Lake geomagnetic excursion (~34 kyr BP), though the
673   details of the timing and structure differ between the two records. Between 32 and 22 kyr BP, model-based estimates
674   of the ^{14}C production rate are ~1.3 times the modern value, which then decrease to around modern levels by HS1 (~18
675   kyr BP).

676

677   Model-based estimates of ^{14}C production during the last glacial are typically higher than paleointensity-based
678   and ice-core ^{10}Be-based ones, as expected from Sect. 3.2. Between 32 and 22 kyr BP, the deconvolutions of the
679   IntCal13 and Hulu Cave $\Delta^{14}C_{atm}$ records give estimates that are about 17.5 percent higher than the reconstructions. It
680   is important to note that the differences between the reconstructions based on proxy data (i.e., paleointensity data and
681   ice-core ^{10}Be fluxes) are as large as the differences between our deconvolution results and the reconstructions (see
682   Table 2). As shown in Fig. 11, it is extremely difficult to reconcile the discrepancies between measurement- and
683   model-based ^{14}C production on the basis of carbon cycle changes alone. Nonetheless, the fact remains that two
684   independent estimates of the ^{14}C production rate (i.e., estimates inferred from paleointensity data and from ice-core
685   ^{10}Be fluxes) show systematically lower rates than those obtained by our model-based deconvolution of $\Delta^{14}C_{atm}$, in
686   particular between 32 and 22 kyr BP. The differences between the production rate results shown in Fig. 10 and Fig.
687   11 and Table 2 stem from various uncertainties that are discussed next.

688

689   Uncertainties associated with the glacial ocean carbon cycle (Fig. 10, colored shading; Fig. 11, colored lines)
690   are systematic in our approach. The deconvolutions, e.g., of the Hulu Cave $\Delta^{14}C_{atm}$ record, under different model
691   scenarios are offset against one another, whereas the millennial-scale variability is maintained (see Fig. 11). We do
692   not attempt to resolve uncertainties associated with Dansgaard-Oeschger warming events and related Antarctic and
693   tropical climatic excursions in the model runs. Such climatic events may have influenced the atmospheric radiocarbon
694   budget, but their influence on long-term variations in $\Delta^{14}C_{atm}$, and therefore inferred production rates, is presumably
695   limited. As may be expected, the lowest production rates (the lowest F_{as} values) are found in VENTx and the highest
696   in scenarios PAL and BIO, mirroring the high and low glacial $\Delta^{14}C_{atm}$ levels achieved by these model scenarios as
697   discussed in Sect. 3.3. Note that there is a large uncertainty in the model-based ^{14}C production rate stemming from

698 uncertainties associated with the reconstruction of past changes in $\Delta^{14}C_{atm}$, in particular the older portion of the $\Delta^{14}C_{atm}$

699 record.

700

701   A shortcoming of paleointensity-based reconstructions of the ^{14}C production rate is that they neglect changes

702 in the solar modulation of the cosmic radiation. The solar modulation potential, which describes the impact of the

703 solar magnetic field on isotope production, varied between 100 and 1200 MeV during the Holocene on decadal to

704 centennial time scales, with a median value of approximately 565 MeV (Roth and Joos, 2013). A halving of the solar

705 modulation potential (e.g., from 600 to 300 MeV) increases the ^{14}C production rate by about 25 percent for the modern

706 geomagnetic field strength (Roth and Joos, 2013; see their Fig. 13). This sensitivity remains similar when changes in

707 the strength of the geomagnetic field are limited as during the last ~35 kyr (Muscheler and Heikkilä, 2011). A shift to

708 lower solar modulation potential could have materialized if the sun spent on average more time in the postulated

709 "Grand Minimum" mode (Usoskin et al., 2014) during the last glacial than during the Holocene. The sensitivity of

710 isotope production to variations in solar modulation potential becomes large during the Laschamp event when the

711 intensity of the geomagnetic field was close to zero and changes in the solar modulation of the cosmic ray flux may

712 have a discernible impact on the high $\Delta^{14}C_{atm}$ levels found over this period. A reduction of the solar modulation

713 potential from 600 to 0 MeV would double ^{14}C production during times of zero geomagnetic field strength (Masarik

714 and Beer, 2009). However, it is likely that changes in the solar modulation potential were insufficient to explain the

715 discrepancy between paleointensity-based production rate estimates and the results of our deconvolution, in particular

716 for the post-Laschamp period and for the reconstruction by Channell et al. (2018). Uncertainties associated with the

717 paleointensity-based reconstructions stem also from uncertainties in estimating the age-scales of the marine sediments

718 and the geomagnetic field data.

719

720   The ice-core ^{10}Be-based reconstruction of past changes in ^{14}C production reflects, by definition, the combined

721 influence of changes in the solar and geomagnetic modulation of the cosmic ray flux reaching the Earth. This method,

722 therefore, avoids a fundamental shortcoming of reconstructions based on geomagnetic field data. The assumption is

723 that the ^{10}Be and ^{36}Cl deposited on polar ice and measured in ice cores scales with the amount of cosmogenic isotopes

724 in the atmosphere. A difficulty is to extrapolate measurements from a single or a few locations to the global

725 atmosphere. Changes in climate influence atmospheric transport and deposition of ^{10}Be as well as the snow

726 accumulation rate, which affect the ice-core ^{10}Be concentration (Elsässer et al., 2015). Furthermore, the sensitivity of

727 ^{10}Be in polar ice versus the sensitivity of total production to magnetic field variations, or "polar bias", is a point of

728 debate, but atmospheric transport models (Heikkilae et al., 2009; Field et al., 2006) and data analyses (Bard et al.,

729 1997; Adolphi and Muscheler, 2016; Adolphi et al., 2018) reach different conclusions about its existence and

730 magnitude. If a polar bias was present, it would lead to an underestimation of the geomagnetic modulation of the ice-

731 core ^{10}Be flux, and therefore variations in the ^{10}Be-based ^{14}C production rate would also be underestimated. However,

732 the mismatch of up to ~544 to 558 permil between reconstructed and modelled ^{10}Be-based $\Delta^{14}C_{atm}$ during the last

733 glacial (see Fig. 7c) appears to be much too large to be reconciled by considering uncertainties in the polar bias alone.

734 Furthermore, this mismatch with reconstructed $\Delta^{14}C_{atm}$ is qualitatively similar when using paleointensity-based ^{14}C

735 production rates that do not suffer from a polar bias (Fig. 7c).

736

737 Given the uncertainties associated with the proxy records, it may not be surprising that estimates of the ^{14}C

738 production rate for the last 50 kyr, as obtained by three fundamentally different methods (geomagnetic field data from

739 marine sediments, ^{10}Be and ^{36}Cl measurements in polar ice cores, and model-based deconvolution of $\Delta^{14}C_{atm}$), disagree

740 with one another, typically by order 10 percent and sometimes by up to 100 percent. At the same time, it is intriguing

741 that two independent estimates of the ^{14}C production rate (i.e., estimates inferred from paleointensity and ice-core ^{10}Be

742 data) give values that are systematically lower than what is required to match the $\Delta^{14}C_{atm}$ reconstruction.

743

744 **4 Summary and conclusions**

745

746 It is generally assumed that $\Delta^{14}C_{atm}$ is controlled by abiotic processes such as atmospheric ^{14}C production, air-sea gas

747 exchange, and ocean circulation and mixing. Here, results from sensitivity experiments with the Bern3D earth system

748 model of intermediate complexity suggest that $\Delta^{14}C_{atm}$ is potentially quite sensitive to the interaction with the ocean

749 sediments on multimillennial time scales. This rather surprising result is due to the coupling of ocean circulation and

750 the sedimentation of biogenic material on the sea floor via the biological carbon pump, which has important

751 implications for the ocean carbon inventory. If the model's ocean carbon cycle is sufficiently perturbed, e.g., by

752 changing the inputs or parameters controlling ocean circulation and/or gas exchange, the imbalance between

753 weathering and sedimentation has a significant impact on the total oceanic amount of carbon. On time scales of tens

754 of thousands of years this slow change in the ocean carbon inventory influences the partitioning of $^{14}C/C$ between the

755 ocean and atmosphere, and thus also oceanic $\Delta^{14}C$ and $\Delta^{14}C_{atm}$. This is important information for long-term climate

756 studies and paleoclimate modelling efforts concerning $\Delta^{14}C_{atm}$. Note that the representation of terrestrial weathering

757 and sea floor sedimentation in the Bern3D is necessarily simplified compared to reality. Nonetheless, a change in the

758 ocean carbon inventory linked with the weathering/sedimentation balance should be discussed as one of the potentially

759 important factors affecting $\Delta^{14}C_{atm}$ during the last glacial period.

760

761 The reason for the high $\Delta^{14}C$ values exhibited by the glacial atmosphere is still not clear. In order to

762 investigate potential mechanisms governing glacial $\Delta^{14}C_{atm}$ levels, the Bern3D model is again used as a tool. Results

763 of model simulations forced only by production changes point out that none of the available reconstructions of the ^{14}C

764 production rate can explain the full amplitude of $\Delta^{14}C_{atm}$ change during the last glacial. In order to test the sensitivity

765 of the model results with respect to the ocean carbon cycle state, various model parameters, i.e., different sets of

766 physical and biogeochemical parameters, were "tuned" to match the glacial CO_2 level. From this, we find that $\Delta^{14}C_{atm}$

767 is most sensitive to changes in physical model parameters, in particular those controlling ocean circulation and gas

768 exchange. In order to achieve an $\Delta^{14}C_{atm}$ value close to the glacial level, the gas transfer velocity in the polar regions

769 had to be reduced by 100 percent. If interpreted as being due to a greater extent of permanent sea ice cover, a reduction

770 in polar air-sea exchange efficiency is a possible explanation for high glacial $\Delta^{14}C_{atm}$ levels. Although this hypothesis

771   is compelling, such a scenario is not supported by the proxy records of Antarctic sea ice cover (Gersonde et al., 2005;
772   Allen et al., 2011) and the $^{13}C/^{12}C$ ratio of atmospheric CO_2 (Eggleston et al., 2016).

773

774   Atmospheric $\Delta^{14}C$ that is modelled at any point in time reflects ^{14}C production at that point, as well as the
775   legacy of past production and carbon cycle changes. The question arises as to whether our conclusions are affected by
776   unaccounted legacy effects, e.g., linked to the preindustrial spin-up simulation or model-diagnosed production rates.
777   Transient simulations forced by reconstructed changes in ^{14}C production (Sect. 3.2 and 3.3) are initialized at 70 kyr
778   BP, but their interpretation is restricted to the last 50,000 years of the integration to minimize legacy effects from
779   model spin-up. Available reconstructions of the ^{14}C production rate in relative units (Sect. 2.5) are applied as a scale
780   factor to the preindustrial steady-state absolute value, which is diagnosed by running the Bern3D model to equilibrium
781   under preindustrial boundary conditions. This approach represents an approximation and equilibrium conditions do
782   not fully apply. Indeed, there is a mismatch between reconstructed and modelled $\Delta^{14}C_{atm}$ at the preindustrial (see Fig.
783   8a). This mismatch is on the order of a few percent or less and adjusting the base level of production accordingly
784   would not remove the large mismatch between reconstructed and modelled $\Delta^{14}C_{atm}$ during the last glacial. In addition,
785   the uncertainty in the absolute value of the preindustrial production rate is on the order of 15%, primarily due to the
786   uncertainties in the preindustrial ocean radiocarbon inventory (see Roth and Joos, 2013, Sect. 3.2). This potential
787   systematic bias, however, does not affect our conclusions as we consider normalized production rate changes (see Fig.
788   7, 10, and 11).

789

790   Before model-simulated $\Delta^{14}C_{atm}$ can be taken seriously, it must be demonstrated that the reconstruction of
791   past changes in ^{14}C production is reliable. There is, however, a substantial amount of scatter in the paleointensity-
792   based and ice-core ^{10}Be-based estimates of ^{14}C production. Here we adopt an alternative approach to estimating the
793   ^{14}C production rate, which would indeed benefit from further constraints and lines of supporting evidence. Our
794   deconvolution-based approach assumes that the ^{14}C production rate can be derived from an atmospheric radiocarbon
795   budget, constructed using a prognostic carbon cycle model combined with the $\Delta^{14}C_{atm}$ record. Here, non-equilibrium
796   effects are fully accounted for by transient simulations where $\Delta^{14}C_{atm}$ and CO_2 are prescribed following their
797   reconstructed histories (Sect. 3.4). Yet, these simulations indicate that the discrepancy between measurement- and
798   model-based estimates of the ^{14}C production rate remains for the last glacial (Fig. 10b). This would suggest that
799   unaccounted legacy effects do not significantly affect our conclusions. Our model results imply that the glacial ^{14}C
800   production rate as inferred from paleointensity data and ice-core ^{10}Be fluxes may be underestimated by about 15
801   percent between 32 and 22 kyr BP, a time interval which appears to be an important piece of the glacial-interglacial
802   $\Delta^{14}C_{atm}$ puzzle. Note that our model-based estimates are associated with uncertainties arising from the reconstruction
803   of the older portion of the $\Delta^{14}C_{atm}$ record and from the model simulation of the glacial ocean carbon cycle (e.g.,
804   uncertainties in the glacial ocean circulation and air-sea CO_2 fluxes). An improved understanding of the role of ^{14}C
805   production in past changes of $\Delta^{14}C_{atm}$ would open up the possibility of attributing model deficiencies to real changes
806   in the ocean carbon cycle, but there is as yet no emerging single record of the ^{14}C production rate.

807

808   Progress in several different areas may help to resolve the glacial-interglacial radiocarbon problem.
809   Additional records of glacial $\Delta^{14}C_{atm}$ would help refine the older portion of the IntCal $\Delta^{14}C$ record. Cosmogenic isotope
810   production records may be improved, e.g., by refining estimates of ice accumulation, by developing a better
811   understanding of ^{10}Be transport and deposition during the glacial, by recovering additional long and continuous
812   records from Antarctic ice cores and including marine ^{10}Be records, and by obtaining additional geomagnetic field
813   data. An expanded spatiotemporal observational coverage of $\Delta^{14}C$ of DIC in the surface and deep ocean would help
814   narrow the time scales of surface-to-deep transport and air-sea equilibration of $\Delta^{14}C$, carbon and nutrients, and thereby
815   guide model-based analyses. Models should become more sophisticated and detailed in order to reproduce
816   successfully the glacial-interglacial changes in carbon and radiocarbon, by including exchange with sediments and the
817   lithosphere and by better representing coastal processes, and by representing a wide variety of paleo proxies such as
818    $\delta^{13}C$, Nd isotopes, carbonate ion concentration, lysocline evolution, and paleo-productivity proxies in a 3-D dynamic
819   context for model evaluation. What is also missing are methods to quantify how the ocean carbon inventory, which
820   co-determines the $^{14}C/C$ ratio and thus the $\Delta^{14}C$ values in the ocean and atmosphere, has changed over the last 50,000
821   years. Ultimately, an improved knowledge of ^{14}C production during the last glacial, as well as more robust constraints
822   on the prevailing climate conditions (e.g., ocean circulation, sea ice cover, and wind speed), are necessary to elucidate
823   the processes permitting mysteriously high $\Delta^{14}C$ levels in the glacial atmosphere.
824
825   **Appendix A: Description of the Bern3D model**
826
827   The physical core of the Bern3D model is based on the 3-D rigid-lid ocean model of Edwards et al. (1998) as updated
828   by Edwards and Marsh (2005). The forcing fields for the model integration are monthly mean wind stress data taken
829   from NCEP/NCAR (Kalnay et al., 1996). Diapycnal mixing is parameterized with a uniform vertical diffusivity K_V of
830   2×10^{-5} m s^{-1}. The parameterization of eddy-induced transport is separated from that of isopycnal mixing, using the
831   Gent-McWilliams skew flux (Griffies, 1998). Running at the same temporal and horizontal resolution, the one-layer
832   energy-moisture balance atmosphere model performs an analysis of the energy budget of the Earth by involving solar
833   radiation, infrared fluxes, evaporation and precipitation, and sensible and latent heat. The zonally averaged surface
834   albedo climatology is taken from Kukla and Robinson (1980). Transport of moisture is performed by diffusion and
835   advection and heat by eddy diffusion.
836
837   The Bern3D ocean carbon cycle model is based on the Ocean Carbon-Cycle Model Intercomparison Project
838   (OCMIP-2) protocols. Air-sea gas exchange is parameterized using the standard gas transfer formulation adopted for
839   OCMIP-2, except that the gas transfer velocity k_w parameterization is a linear function of wind speed (Krakauer et
840   al., 2006) to which we have added a scale factor of 0.81 to match the observed global ocean inventory of bomb ^{14}C
841   (Müller et al., 2008). It is assumed that CO_2 and O_2 are well-mixed in the atmosphere. Surface boundary conditions
842   also include a virtual-flux term for biogeochemical tracers (e.g., DIC and Alk) to account for their dilution or
843   concentration due to implicit freshwater fluxes. Following OCMIP-2 biotic protocol, new production is partitioned
844   into particulate and dissolved organic matter. Modifications from the original OCMIP-2 biotic protocol include the

845 prognostic formulation of new/export production as a function of light, temperature, and limiting nutrient
846 concentrations, where the nutrient uptake follows Michaelis-Menten kinetics. The production of biogenic $CaCO_3$ and
847 opal is computed on the basis of the modelled particulate organic carbon (POC) production and availability of silicate,
848 with a maximum possible fraction of $CaCO_3$ material that can be produced. This threshold value is represented by the
849 $CaCO_3$-to-POC export ratio. In the preindustrial control run, the global mean export ratio rr is 0.082.

850

851 Biogenic particles that have been produced in the 75-m production zone are redistributed over the water
852 column in order to parameterize the downward particle flux through the water column. A power-law model referred
853 to as the Martin curve is used to describe the vertical POC flux profile, whereas both $CaCO_3$ and opal export are
854 redistributed over the water column with an exponential curve. POC is remineralized instantaneously back to dissolved
855 form according to Redfield stoichiometry and with a 250–m length scale l_{POC} (i.e., in 250 m, the POC flux declines
856 by $1 - 1/e \approx 63$ percent). Likewise, $CaCO_3$ and opal are dissolved within one time step, with e-folding depths of
857 5066 and 10,000 m, respectively. Biogenic particles reaching the model's sea floor form the upper boundary condition
858 of the 10-layer sediment model after Heinze et al. (1999) and Gehlen et al. (2006). The sediment model includes four
859 solid sediment components (POC, $CaCO_3$, opal, and clay) and is based on the sediment advection and accumulation
860 scheme as in the work of Archer et al. (1993). The rate of POC remineralization in the sediments is primarily
861 determined by the pore water concentration of oxygen, whereas the mineral dissolution rate is governed by the
862 saturation state of sediment pore waters with respect to $CaCO_3$ or opal. Weathering (dissolution) of carbonate and
863 silicate rocks on land, phosphorous release by chemical weathering of rocks, and volcanic outgassing of CO_2 are
864 simulated as constant inputs of DIC, Alk (as bicarbonate ion, HCO_3^-), phosphate (P), and silicate (Si) to the ocean at
865 rates intended to balance their removal from the ocean by sedimentation on the sea floor. These weathering inputs are
866 added as a constant increment to each surface ocean grid cell along the coastlines. The preindustrial steady state of
867 the model is used to diagnose the weathering rates that are held fixed and constant throughout the simulations. Note
868 that the preindustrial spin-up results in steady-state values for weathering-derived inputs of DIC, Alk, P, and Si of
869 0.46 Gt C per year, 34.37 Tmol HCO_3^- per year, 0.17 Tmol P per year, and 6.67 Tmol Si per year, respectively. These
870 values are within the range of observational estimates (see, e.g., Jeltsch-Thömmes et al., 2019). Additional details
871 concerning the sediment model are provided in Tschumi et al. (2011), while the appendix of Jeltsch-Thömmes et al.
872 (2019) gives a detailed description of the atmosphere–ocean–sediment spin-up.

873

874 The exchange of any isotopic perturbation between the atmosphere and the terrestrial biosphere is simulated
875 by use of the four-box model of Siegenthaler and Oeschger (1987). The terrestrial biosphere is represented by four
876 well-mixed compartments (ground vegetation plus leaves, wood, detritus, and soils), with a fixed total carbon
877 inventory of 2220 Gt C. Net primary production is balanced by respiration of detritus and soils, and is set to 60 Gt C
878 per year.

879

References

Adolphi, F., and Muscheler, R.: Synchronizing the Greenland ice core and radiocarbon timescales over the Holocene – Bayesian wiggle-matching of cosmogenic radionuclide records, Climate of the Past, 12, 15–30, 2016.

Adolphi, F., Muscheler, R., Svensson, A., Aldahan, A., Possnert, G., Beer, J., . . . Thiéblemont, R.: Persistent link between solar activity and Greenland climate during the Last Glacial Maximum, Nature Geoscience, 7, 662–666, 2014.

Adolphi, F., Ramsey, C. B., Erhardt, T., Edwards, R. L., Cheng, H., Turney, C. S., . . . Muscheler, R.: Connecting the Greenland ice-core and U/Th timescales via cosmogenic radionuclides: testing the synchroneity of Dansgaard–Oeschger events, Climate of the Past, 14, 1755–1781, 2018.

Allen, C. S., Pike, J., and Pudsey, C. J.: Last glacial–interglacial sea-ice cover in the SW Atlantic and its potential role in global deglaciation, Quaternary Science Reviews, 30, 2446–2458, 2011.

Archer, D., and Maier-Reimer, E.: Effect of deep-sea sedimentary calcite preservation on atmospheric CO_2 concentration, Nature, 367, 260–263, 1994.

Archer, D., Lyle, M., Rodgers, K., and Froelich, P.: What controls opal preservation in tropical deep-sea sediments?, Paleoceanography, 8, 7–21, 1993.

Archer, D., Winguth, A., Lea, D., and Mahowald, N.: What caused the glacial/interglacial atmospheric pCO_2 cycles?, Reviews of Geophysics, 38, 159–189, 2000.

Audi, G., Bersillon, O., Blachot, J., and Wapstra, A. H.: The Nubase evaluation of nuclear and decay properties, Nuclear Physics A, 729, 3–128, 2003.

Bard, E., Raisbeck, G. M., Yiou, F., and Jouzel, J.: Solar modulation of cosmogenic nuclide production over the last millennium: comparison between ^{14}C and ^{10}Be records, Earth and Planetary Science Letters, 150, 453–462, 1997.

917   Baumgartner, S., Beer, J., Wagner, G., Kubik, P., Suter, M., Raisbeck, G. M., and Yiou, F.: [10]Be and dust, Nuclear
918   Instruments and Methods in Physics Research Section B: Beam Interactions with Materials and Atoms,
919   123, 296–301, 1997.

920   Baumgartner, S., Beer, J., Masarik, J., Wagner, G., Meynadier, L., and Synal, H.-A.: Geomagnetic Modulation of
921   the [36]Cl Flux in the GRIP Ice Core, Greenland, Science, 279, 1330–1332, 1998.

922   Bé, M.-M., Chisté, V., Dulieu, C., Mougeot, X., Chechev, V., Kondev, F., . . . Wang, B.: Table of Radionuclides
923   (Comments on evaluations), Monographie BIPM-5, 7, 2013.

924   Berger, A. L.: Long-term variations of daily insolation and Quaternary climatic changes, Journal of the Atmospheric
925   Sciences, 35, 2362–2367, 1978.

926   Broecker, W., and Barker, S.: A 190‰ drop in atmosphere's Δ^{14}C during the "Mystery Interval" (17.5 to 14.5 kyr),
927   Earth and Planetary Science Letters, 256, 90–99, 2007.

928   Broecker, W. S., and Peng, T.-H.: Gas exchange rates between air and sea, Tellus, 26, 21–35, 1974.

929   Bronk Ramsey, C., Staff, R. A., Bryant, C. L., Brock, F., Kitagawa, H., van der Plicht, J., Schlolaut, G., Marshall,
930   M. H., Brauer, A., Lamb, H. F., Payne, R. L., Tarasov, P. E., Haraguchi, T., Gotanda, K., Yonenobu, H.,
931   Yokoyama, Y., Tada, R., and Nakagawa, T.: A complete terrestrial radiocarbon record for 11.2 to 52.8 kyr
932   B.P., Science, 338, 370–374, 2012.

933   Brovkin, V., Ganopolski, A., Archer, D., and Munhoven, G.: Glacial CO_2 cycle as a succession of key physical and
934   biogeochemical processes, Climate of the Past, 8, 251–264, 2012.

935   Butzin, M., Köhler, P., and Lohmann, G.: Marine radiocarbon reservoir age simulations for the past 50,000 years,
936   Geophysical Research Letters, 44, 8473–8480, 2017.

937   Channell, J. E., Hodell, D. A., Crowhurst, S. J., Skinner, L. C., and Muscheler, R.: Relative paleointensity (RPI) in
938   the latest Pleistocene (10-45 ka) and implications for deglacial atmospheric radiocarbon, Quaternary
939   Science Reviews, 191, 57–72, 2018.

940   Cheng, H., Edwards, R. L., Southon, J., Matsumoto, K., Feinberg, J. M., Sinha, A., . . . Ning, Y.: Atmospheric
941   ^{14}C/^{12}C changes during the last glacial period from Hulu Cave, Science, 362, 1293–1297, 2018.

942   Delaygue, G., Stocker, T. F., Joos, F., and Plattner, G.-K.: Simulation of atmospheric radiocarbon during abrupt
943   oceanic circulation changes: trying to reconcile models and reconstructions, Quaternary Science Reviews,
944   22, 1647–1658, 2003.

945   Edwards, N. R., and Marsh, R.: Uncertainties due to transport-parameter sensitivity in an efficient 3-D ocean-
946   climate model, Climate Dynamics, 24, 415–433, 2005.

947   Edwards, N. R., Willmott, A. J., and Killworth, P. D.: On the Role of Topography and Wind Stress on the Stability
948   of the Thermohaline Circulation, Journal of Physical Oceanography, 28, 756–778, 1998.

949   Eggleston, S., Schmitt, J., Bereiter, B., Schneider, R., and Fischer, H.: Evolution of the stable carbon isotope
950   composition of atmospheric CO_2 over the last glacial cycle, Paleoceanography, 31, 434–452, 2016.

951   Elsässer, C., Wagenbach, D., Levin, I., Stanzick, A., Christl, M., Wallner, A., . . . Dibb, J.: Simulating ice core [10]Be
952   on the glacial–interglacial timescale, Climate of the Past, 11, 115–133, 2015.

953 Enting, I. G.: On the use of smoothing splines to filter CO_2 data, Journal of Geophysical Research, 92, 10,977–
954   10,984, 1987.

955 Field, C. V., Schmidt, G. A., Koch, D., and Salyk, C.: Modeling production and climate-related impacts on [10]Be
956   concentration in ice cores, Journal of Geophysical Research: Atmospheres, 111,
957   https://doi.org/10.1029/2005JD006410, 2006.

958 Finkel, R. C., and Nishiizumi, K.: Beryllium 10 concentrations in the Greenland Ice Sheet Project 2 ice core from 3-
959   40 ka, Journal of Geophysical Research: Oceans, 102, 26699–26706, 1997.

960 Fischer, H., Schmitt, J., Lüthi, D., Stocker, T. F., Tschumi, T., Parekh, P., . . . Wolff, E.: The role of Southern Ocean
961   processes in orbital and millennial CO_2 variations – A synthesis, Quaternary Science Reviews, 29, 193–
962   205, 2010.

963 Galbraith, E. D., and Skinner, L. C.: The Biological Pump During the Last Glacial Maximum, Annual Review of
964   Marine Science, 12, 559–586, 2020.

965 Ganopolski, A., and Brovkin, V.: Simulation of climate, ice sheets and CO_2 evolution during the last four glacial
966   cycles with an Earth system model of intermediate complexity, Climate of the Past, 13, 1695–1716, 2017.

967 Gehlen, M., Bopp, L. E., Aumont, O., Heinze, C., and Ragueneau, O.: Reconciling surface ocean productivity,
968   export fluxes and sediment composition in a global biogeochemical ocean model, Biogeosciences, 3, 521–
969   537, 2006.

970 Gersonde, R., Crosta, X., Abelmann, A., and Armand, L.: Sea-surface temperature and sea ice distribution of the
971   Southern Ocean at the EPILOG Last Glacial Maximum—a circum-Antarctic view based on siliceous
972   microfossil records, Quaternary Science Reviews, 24, 869–896, 2005.

973 Gkinis, V., Simonsen, S. B., Buchardt, S. L., White, J. W., and Vinther, B. M.: Water isotope diffusion rates from
974   the NorthGRIP ice core for the last 16,000 years – Glaciological and paleoclimatic implications, Earth and
975   Planetary Science Letters, 405, 132–141, 2014.

976 Griffies, S. M.: The Gent-McWilliams Skew Flux, Journal of Physical Oceanography, 28, 831–841, 1998.

977 Hain, M. P., Sigman, D. M., and Haug, G. H.: Distinct roles of the Southern Ocean and North Atlantic in the
978   deglacial atmospheric radiocarbon decline, Earth and Planetary Science Letters, 394, 198–208, 2014.

979 Heikkilä, U., Beer, J., and Feichter, J.: Meridional transport and deposition of atmospheric [10]Be, Atmospheric
980   Chemistry and Physics, 9, 515–527, 2009.

981 Heikkilä, U., Phipps, S. J., and Smith, A. M.: [10]Be in late deglacial climate simulated by ECHAM5-HAM – Part 1:
982   Climatological influences on [10]Be deposition, Climate of the Past, 9, 2641–2649, 2013.

983 Heinze, C., Maier-Reimer, E., Winguth, A. M., and Archer, D.: A global oceanic sediment model for long-term
984   climate studies, Global Biogeochemical Cycles, 13, 221–250, 1999.

985 Herbst, K., Muscheler, R., and Heber, B.: The new local interstellar spectra and their influence on the production
986   rates of the cosmogenic radionuclides [10]Be and ^{14}C, Journal of Geophysical Research: Space Physics, 122,
987   23–34, 2017.

988 Hoff, U., Rasmussen, T. L., Stein, R., Ezat, M. M., and Fahl, K.: Sea ice and millennial-scale climate variability in
989   the Nordic seas 90 kyr ago to present, Nature Communications, 7, doi:10.1038/ncomms12247, 2016.

990   Hughen, K., Lehman, S., Southon, J., Overpeck, J., Marchal, O., Herring, C., and Turnbull, J.: [14]C Activity and
991   Global Carbon Cycle Changes over the Past 50,000 Years, Science, 303, 202–207, 2004.

992   Huiskamp, W. N., and Meissner, K. J.: Oceanic carbon and water masses during the Mystery Interval: A model-data
993   comparison study, Paleoceanography and Paleoclimatology, 27, https://doi.org/10.1029/2012PA002368,
994   2012.

995   Jeltsch-Thömmes, A., Battaglia, G., Cartapanis, O., Jaccard, S. L., and Joos, F.: Low terrestrial carbon storage at the
996   Last Glacial Maximum: constraints from multi-proxy data, Climate of the Past, 15, 849–879, 2019.

997   Köhler, P., Muscheler, R., and Fischer, H.: A model-based interpretation of low-frequency changes in the carbon
998   cycle during the last 120,000 years and its implications for the reconstruction of atmospheric Δ^{14}C,
999   Geochemistry Geophysics Geosystems, 7, 1–22, 2006.

1000   Köhler, P., Nehrbass-Ahles, C., Schmitt, J., Stocker, T. F., and Fischer, H.: A 156 kyr smoothed history of the
1001   atmospheric greenhouse gases CO_2, CH_4, and N_2O and their radiative forcing, Earth System Science Data,
1002   9, 363–387, 2017.

1003   Kalnay, E., Kanamitsu, M., Kistler, R., Collins, W., Deaven, D., Gandin, L., . . . Joseph, D.: The NCEP/NCAR 40-
1004   Year Reanalysis Project, Bulletin of the American Meteorological Society, 77, 437–471, 1996.

1005   Key, R. M., Kozyr, A., Sabine, C. L., Lee, K., Wanninkhof, R., Bullister, J. L., . . . Peng, T.-H.: A global ocean
1006   carbon climatology: Results from Global Data Analysis Project (GLODAP), Global Biogeochemical
1007   Cycles, 18, https://doi.org/10.1029/2004GB002247, 2004.

1008   Kovaltsov, G. A., and Usoskin, I. G.: A new 3D numerical model of cosmogenic nuclide [10]Be production in the
1009   atmosphere, Earth and Planetary Science Letters, 291, 182–188, 2010.

1010   Krakauer, N. Y., Randerson, J. T., Primeau, F. W., Gruber, N., and Menemenlis, D.: Carbon isotope evidence for the
1011   latitudinal distribution and wind speed dependence of the air-sea gas transfer velocity, Tellus B: Chemical
1012   and Physical Meteorology, 58, 390–417, 2006.

1013   Kukla, G., and Robinson, D.: Annual Cycle of Surface Albedo, Monthly Weather Review, 108, 56–68, 1980.

1014   Laj, C., Kissel, C., Mazaud, A., Channell, J. E., and Beer, J.: North Atlantic palaeointensity stack since 75ka
1015   (NAPIS-75) and the duration of the Laschamp event, Philosophical Transactions of the Royal Society of
1016   London. Series A: Mathematical, Physical and Engineering Sciences, 358, 1009–1025, 2000.

1017   Laj, C., Kissel, C., Mazaud, A., Michel, E., Muscheler, R., and Beer, J.: Geomagnetic field intensity, North Atlantic
1018   Deep Water circulation and atmospheric Δ^{14}C during the last 50 kyr, Earth and Planetary Science Letters,
1019   200, 177-190, 2002.

1020   Laj, C., Kissel, C., and Beer, J.: High resolution global paleointensity stack since 75 kyr (GLOPIS-75) calibrated to
1021   absolute values, Timescales of the Paleomagnetic Field, 145, 255–265, 2004.

1022   Laj, C., Guillou, H., and Kissel, C.: Dynamics of the earth magnetic field in the 10-75 kyr period comprising the
1023   Laschamp and Mono Lake excursions: New results from the French Chaîne des Puys in a global
1024   perspective, Earth and Planetary Science Letters, 387, 184–197, 2014.

1025   Lisiecki, L. E., and Stern, J. V.: Regional and global benthic δ18O stacks for the last glacial cycle,
1026   Paleoceanography, 31, 1368–1394, 2016.

1027 Müller, J., and Stein, R.: High-resolution record of late glacial and deglacial sea ice changes in Fram Strait
1028   corroborates ice–ocean interactions during abrupt climate shifts, Earth and Planetary Science Letters, 403,
1029   446–455, 2014.

1030 Müller, S. A., Joos, F., Edwards, N. R., and Stocker, T. F.: Water Mass Distribution and Ventilation Time Scales in
1031   a Cost-Efficient, Three-Dimensional Ocean Model, Journal of Climate, 19, 5479–5499, 2006.

1032 Müller, S. A., Joos, F., Plattner, G.-K., Edwards, N. R., and Stocker, T. F.: Modeled natural and excess radiocarbon:
1033   Sensitivities to the gas exchange formulation and ocean transport strength, Global Biogeochemical Cycles,
1034   22, https://doi.org/10.1029/2007GB003065, 2008.

1035 Marchal, O., Stocker, T. F., and Muscheler, R.: Atmospheric radiocarbon during the Younger Dryas: production,
1036   ventilation, or both?, Earth and Planetary Science Letters, 185, 383–395, 2001.

1037 Mariotti, V., Paillard, D., Bopp, L., Roche, D. M., and Bouttes, N.: A coupled model for carbon and radiocarbon
1038   evolution during the last deglaciation, Geophysical Research Letters, 43, 1306–1313, 2016.

1039 Masarik, J., and Beer, J.: Simulation of particle fluxes and cosmogenic nuclide production in the Earth's atmosphere,
1040   Journal of Geophysical Research: Atmospheres, 104, 12099–12111, 1999.

1041 Masarik, J., and Beer, J.: An updated simulation of particle fluxes and cosmogenic nuclide production in the Earth's
1042   atmosphere, Journal of Geophysical Research: Atmospheres, 114, https://doi.org/10.1029/2008JD010557,
1043   2009.

1044 Menviel, L., Joos, F., and Ritz, S. P.: Simulating atmospheric CO_2, ^{13}C and the marine carbon cycle during the Last
1045   Glacial–Interglacial cycle: possible role for a deepening of the mean remineralization depth and an increase
1046   in the oceanic nutrient inventory, Quaternary Science Reviews, 56, 46–68, 2012.

1047 Muscheler, R., and Heikkilä, U.: Constraints on long-term changes in solar activity from the range of variability of
1048   cosmogenic radionuclide records, Astrophysics and Space Sciences Transactions, 7, 355–364, 2011.

1049 Muscheler, R., Beer, J., Wagner, G., Laj, C., Kissel, C., Raisbeck, G. M., . . . Kubike, P. W.: Changes in the carbon
1050   cycle during the last deglaciation as indicated by the comparison of ^{10}Be and ^{14}C records, Earth and
1051   Planetary Science Letters, 219, 325–340, 2004.

1052 Muscheler, R., Adolphi, F., Herbst, K., and Nilsson, A.: The Revised Sunspot Record in Comparison to Cosmogenic
1053   Radionuclide-Based Solar Activity Reconstructions, Solar Physics, 291, 3025–3043, 2016.

1054 Nowaczyk, N. R., Arz, H. W., Frank, U., Kind, J., and Plessen, B.: Dynamics of the Laschamp geomagnetic
1055   excursion from Black Sea sediments, Earth and Planetary Science Letters, 351-352, 54–69, 2012.

1056 Nowaczyk, N. R., Frank, U., Kind, J., and Arz, H. W.: A high-resolution paleointensity stack of the past 14 to 68 ka
1057   from Black Sea sediments, Earth and Planetary Science Letters, 384, 1–16, 2013.

1058 Orr, J. C., Najjar, R. G., Aumont, O., Bopp, L., Bullister, J. L., Danabasoglu, G., . . . Yool, A.: Biogeochemical
1059   protocols and diagnostics for the CMIP6 Ocean Model Intercomparison Project (OMIP), Geoscientific
1060   Model Development, 10, 2169–2199, 2017.

1061 Parekh, P., Joos, F., and Müller, S. A.: A modeling assessment of the interplay between aeolian iron fluxes and iron-
1062   binding ligands in controlling carbon dioxide fluctuations during Antarctic warm events, Paleoceanography
1063   and Paleoclimatology, 23, https://doi.org/10.1029/2007PA001531, 2008.

Peltier, W. R.: Ice Age Paleotopography, Science, 265, 195–201, 1994.

Poluianov, S. V., Kovaltsov, G. A., Mishev, A. L., and Usoskin, I. G.: Production of cosmogenic isotopes [7]Be, [10]Be, ^{14}C, [22]Na, and [36]Cl in the atmosphere: Altitudinal profiles of yield functions, Journal of Geophysical Research: Atmospheres, 121, 8125–8136, 2016.

Potgieter, M. S., Vos, E. E., Boezio, M., De Simone, N., Di Felice, V., and Formato, V.: Modulation of Galactic Protons in the Heliosphere During the Unusual Solar Minimum of 2006 to 2009, Solar Physics, 289, 391–406, 2014.

Primeau, F.: Characterizing Transport between the Surface Mixed Layer and the Ocean Interior with a Forward and Adjoint Global Ocean Transport Model, Journal of Physical Oceanography, 35, 545–564, 2005.

Raisbeck, G. M., Cauquoin, A., Jouzel, J., Landais, A., Petit, J.-R., Lipenkov, V. Y., . . . Yiou, F.: An improved north-south synchronization of ice core records around the 41 kyr [10]Be peak, Climate of the Past, 13, 217–229, 2017.

Rasmussen, S. O., Abbott, P. M., Blunier, T., Bourne, A. J., Brook, E. J., Buchardt, S. L., . . . Winstrup, M.: A first chronology for the North Greenland Eemian Ice Drilling (NEEM) ice core, Climate of the Past, 9, 2713–2730, 2013.

Reimer, P., Bard, E., Bayliss, A., Beck, J., Blackwell, P., Ramsey, C., . . . Van der Plicht, J.: IntCal13 and Marine13 Radiocarbon Age Calibration Curves 0-50,000 Years cal BP, Radiocarbon, 55, 1869–1887, 2013.

Reimer, P., Austin, W.E.N., Bard, E., Bayliss, A., Blackwell, P. G., Ramsey, C. B., . . . Talamo, S.: The IntCal20 Northern Hemisphere radiocarbon age calibration curve (0-55 kcal BP), Radiocarbon, in press.

Ritz, S. P., Stocker, T. F., and Joos, F.: A Coupled Dynamical Ocean–Energy Balance Atmosphere Model for Paleoclimate Studies, Journal of Climate, 24, 349–375, 2011.

Roth, R., and Joos, F.: A reconstruction of radiocarbon production and total solar irradiance from the Holocene ^{14}C and CO_2 records: implications of data and model uncertainties, Climate of the Past, 9, 1879–1909, 2013.

Roth, R., Ritz, S. P., and Joos, F.: Burial-nutrient feedbacks amplify the sensitivity of atmospheric carbon dioxide to changes in organic matter remineralisation, Earth System Dynamics, 5, 321–343, 2014.

Sarnthein, M., Schneider, B., and Grootes, P. M.: Peak glacial ^{14}C ventilation ages suggest major draw-down of carbon into the abyssal ocean, Climate of the Past, 9, 2595–2614, 2013.

Siegenthaler, U., and Oeschger, H.: Biospheric CO_2 emissions during the past 200 years reconstructed by deconvolution of ice core data, Tellus, 39B, 140–154, 1987.

Siegenthaler, U., Heimann, M., and Oeschger, H.: [14]C Variations Caused by Changes in the Global Carbon Cycle, Radiocarbon, 22, 177–191, 1980.

Skinner, L. C., Fallon, S., Waelbroeck, C., Michel, E., and Barker, S.: Ventilation of the Deep Southern Ocean and Deglacial CO_2 Rise, Science, 328, 1147–1151, 2010.

Skinner, L. C., Primeau, F., Freeman, E., de la Fuente, M., Goodwin, P. A., Gottschalk, J., . . . Scrivner, A. E.: Radiocarbon constraints on the glacial ocean circulation and its impact on atmospheric CO_2, Nature Communications, 8, doi:10.1038/ncomms16010, 2017.

1100 Skinner, L. C., Muschitiello, F., and Scrivner, A. E.: Marine Reservoir Age Variability Over the Last Deglaciation:
1101   Implications for Marine Carbon Cycling and Prospects for Regional Radiocarbon Calibrations,
1102   Paleoceanography and Paleoclimatology, 34, 1807–1815, 2019.
1103 Soulet, G., Skinner, L. C., Beaupré, S. R., and Galy, V.: A Note on Reporting of Reservoir ^{14}C Disequilibria and
1104   Age Offsets, Radiocarbon, 58, 205–211, 2016.
1105 Southon, J., Noronha, A. L., Cheng, H., Edwards, R. L., and Wang, Y.: A high-resolution record of atmospheric ^{14}C
1106   based on Hulu Cave speleothem H82, Quaternary Science Reviews, 33, 32–41, 2012.
1107 Stuiver, M., and Polach, H. A.: Discussion: Reporting of ^{14}C Data, Radiocarbon, 19, 355–363, 1977.
1108 Tschumi, T., Joos, F., and Parekh, P.: How important are Southern Hemisphere wind changes for low glacial carbon
1109   dioxide? A model study, Paleoceanography and Paleoclimatology, 23,
1110   https://doi.org/10.1029/2008PA001592, 2008.
1111 Tschumi, T., Joos, F., Gehlen, M., and Heinze, C.: Deep ocean ventilation, carbon isotopes, marine sedimentation
1112   and the deglacial CO_2 rise, Climate of the Past, 7, 771–800, 2011.
1113 Usoskin, I. G., Hulot, G., Gallet, Y., Roth, R., Licht, A., Joos, F., . . . Khokhlov, A.: Evidence for distinct modes of
1114   solar activity, Astronomy & Astrophysics, 562, 1–4, 2014.
1115 Wagner, G., Beer, J., Masarik, J., Muscheler, R., Kubik, P. W., Mende, W., . . . Yiou, F.: Presence of the solar de
1116   Vries cycle (~205 years) during the last ice age, Geophysical Research Letters, 28, 303–306, 2001.
1117 Wallmann, K., Schneider, B., and Sarnthein, M.: Effects of eustatic sea-level change, ocean dynamics, and nutrient
1118   utilization on atmospheric pCO_2 and seawater composition over the last 130 000 years: a model study,
1119   Climate of the Past, 12, 339–375, 2016.
1120 Yiou, F., Raisbeck, G. M., Baumgartner, S., Beer, J., Hammer, C., Johnsen, S., . . . Yiou, P.: Beryllium 10 in the
1121   Greenland Ice Core Project ice core at Summit, Greenland, Journal of Geophysical Research: Oceans, 102,
1122   26783–26794, 1997.
1123
1124
1125
1126
1127
1128
1129
1130
1131
1132
1133
1134
1135
1136

1137
1138

1139 Table 1. Summary of model scenarios considered in this study. Initial conditions refer to the boundary conditions used
1140 for the precursor spin-up simulation needed to initialize the transient simulation. These correspond either to
1141 preindustrial (PI) or last glacial conditions. The paleoclimate forcing fields, i.e., Orb-GHG-Ice, are reconstructed
1142 changes in orbital parameters (Berger, 1978), greenhouse gas radiative forcing based on reconstructed atmospheric
1143 greenhouse gas histories (Köhler et al., 2017), and varying ice sheet extent scaled using the global benthic δ^{18}O stack
1144 of Lisiecki and Stern (2016). Numbers refer to the scale factor values applied to the tunable model parameters τ (wind
1145 stress scale factor), K_V (vertical diffusivity), k_w (gas transfer velocity), rr (CaCO$_3$-to-POC export ratio), and ℓ_{POC}
1146 (POC remineralization length scale) at the last glacial maximum (LGM). These values were chosen in order to achieve
1147 an atmospheric CO$_2$ concentration close to the LGM level, and are varied over time using the global benthic δ^{18}O
1148 stack. See Roth et al. (2014) for the Bern3D model parameter set. In all scenarios, the fully coupled model
1149 configuration, including the major global carbon reservoirs (atmosphere, terrestrial biosphere, ocean, and sediments),
1150 is used.

Scenario	Initial conditions	Paleoclimate forcing	Tunable parameters: scale factor at LGM				
			τ	K_V	k_w	rr	ℓ_{POC}
MOD	PI	-	-	-	-	-	-
PAL	Glacial	Orb-GHG-Ice	-	-	-	-	-
CIRC	Glacial	Orb-GHG-Ice	0.4	0.4	-	-	-
VENT	Glacial	Orb-GHG-Ice	0.4	0.4	0.4	-	-
VENTx	Glacial	Orb-GHG-Ice	0.4	0.4	0.0	-	-
BIO	Glacial	Orb-GHG-Ice	-	-	-	0.8	1.2
PHYS-BIO	Glacial	Orb-GHG-Ice	0.7	0.7	0.7	0.7	-
PHYS-BIOx	Glacial	Orb-GHG-Ice	0.8	0.8	0.8	0.8	1.2

1151
1152
1153
1154
1155
1156
1157

1158
1159
1160
1161

1162   Table 2. Production rate estimates in relative units inferred from three fundamentally different reconstruction methods:
1163   geomagnetic field data from marine sediments, [10]Be and [36]Cl measurements in polar ice cores, and model-based
1164   deconvolution of atmospheric Δ^{14}C. Laj00, Laj04, Now13, and Chn18 refer to the paleointensity-based reconstructions
1165   of Laj et al. (2000), Laj et al. (2004), Nowaczyk et al. (2013), and Channell et al. (2018), respectively. Adp18 refers
1166   to the ice-core [10]Be-based reconstruction of Adolphi et al. (2018). Int13 and Hul18 refer to the model-based
1167   reconstructions from this study, using the IntCal13 calibration curve (Reimer et al., 2013) and the new Hulu Cave
1168 Δ^{14}C dataset (Cheng et al., 2018). The bold numbers show the mean production rates during the last glacial (50 to 18
1169   kyr BP).

Time (kyr BP)	Mean production rate (relative units)						
	Laj00	Laj04	Now13	Chn18	Adp18	Int13	Hul18
50 to 42	1.08	1.04	1.12	1.08	1.01	1.23	1.14
42 to 37	1.57	1.56	1.71	1.36	1.44	1.45	1.67
37 to 32	1.19	1.09	1.35	0.98	1.10	1.25	1.28
32 to 22	1.22	1.15	1.29	0.92	0.99	1.31	1.31
22 to 18	1.31	1.20	1.17	0.81	0.98	1.11	1.11
50 to 18	**1.25**	**1.18**	**1.31**	**1.01**	**1.08**	**1.28**	**1.29**

1170
1171
1172
1173
1174
1175
1176
1177
1178
1179
1180
1181
1182
1183
1184
1185
1186
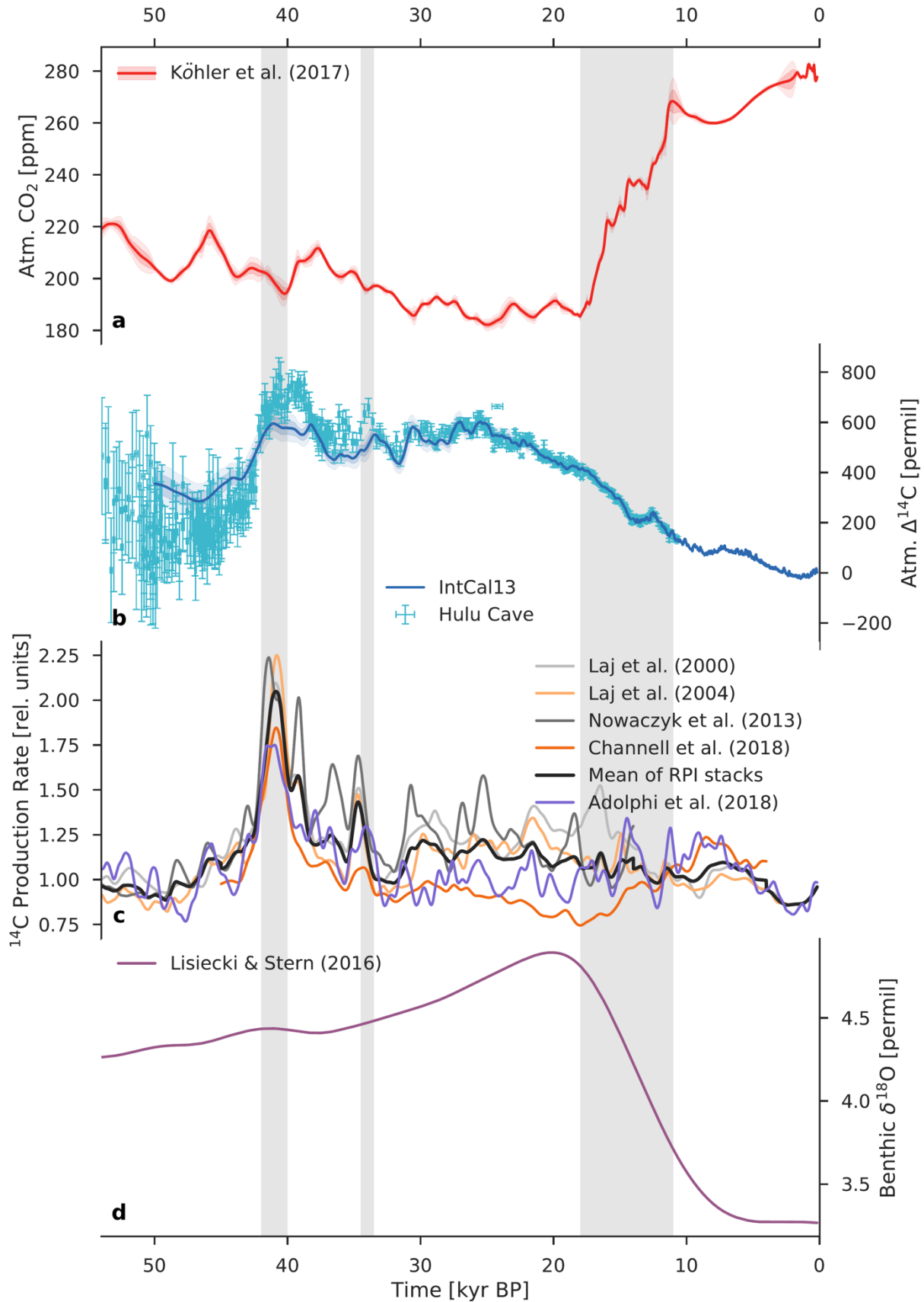
Fig. 1. Comparison of various paleoclimate records for the last 54 kyr. (a) Atmospheric CO_2 from the data compilation of Köhler et al. (2017). The light red envelope shows the uncertainty (2σ). (b) Atmospheric $\Delta^{14}C$ reconstructed from ^{14}C measurements on tree rings, plant macrofossils, speleothems, corals, and foraminifera. The light blue envelope shows the uncertainty (2σ) in the IntCal13 calibration curve (Reimer et al., 2013), whereas the Hulu Cave data (Cheng et al., 2018) are shown with error bars (1σ). Hulu Cave data are consistent with IntCal13 between ~10.6 and 33.3 kyr BP. For both records $\Delta^{14}C$ values were adjusted to the presently accepted value of the radiocarbon half-life (5700 years). (c) ^{14}C production rate in relative units reconstructed from paleointensity data (Laj et al., 2000; Laj et al., 2004; Nowaczyk et al., 2013; Channell et al., 2018) and from polar ice-core ^{10}Be fluxes (Adolphi et al., 2018). The heavy dark gray line is the mean paleointensity-based ^{14}C production rate. (d) Global benthic $\delta^{18}O$ stack, a proxy for ice volume, from Lisiecki and Stern (2016). Three vertical light gray bars indicate the Laschamp excursion (~41 kyr BP), when the Earth's geomagnetic dipole field intensity was close to zero, the Mono Lake geomagnetic excursion (~34 kyr BP), and the last glacial termination (~18 to 11 kyr BP), respectively.
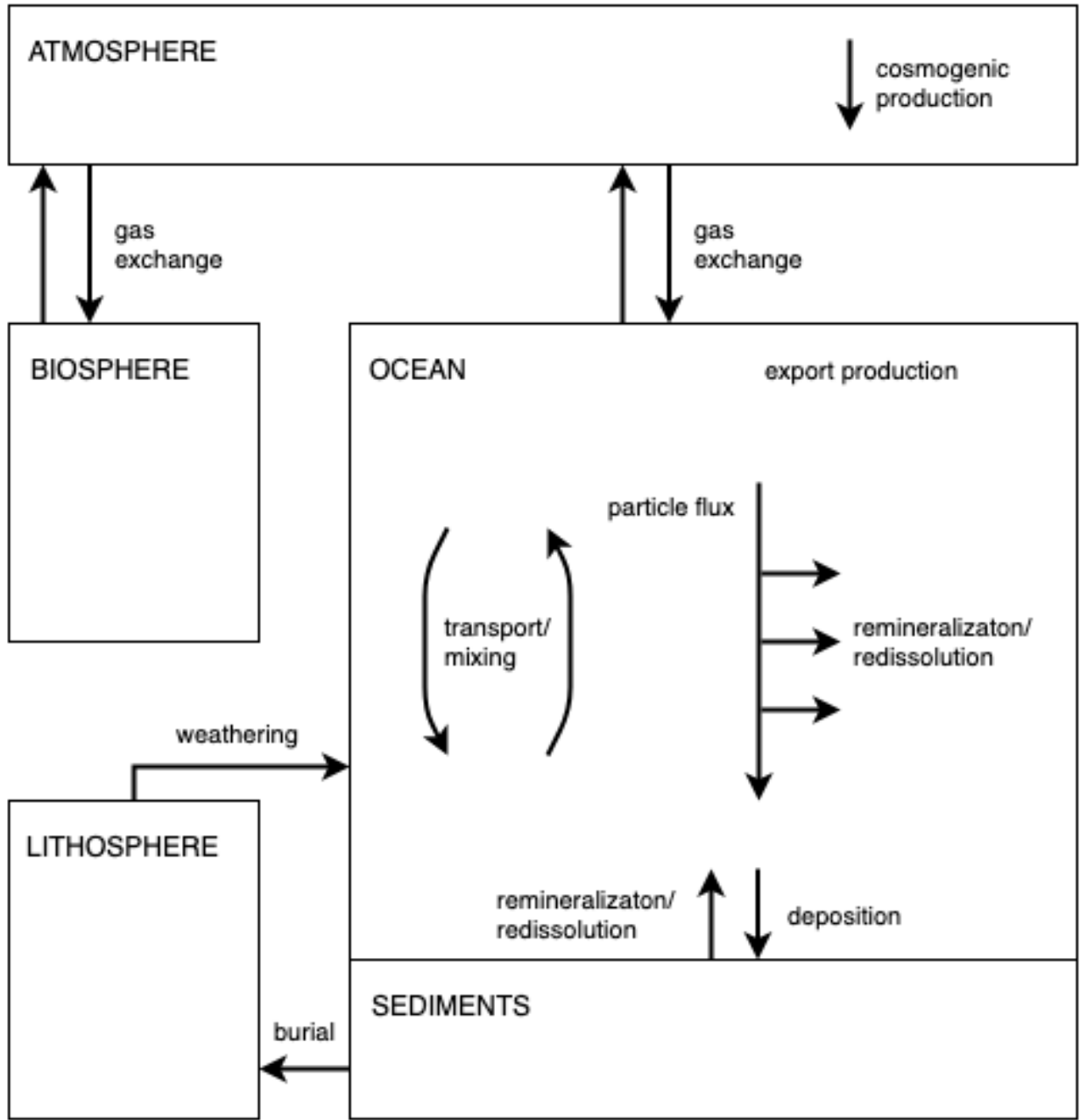
1217
1218   Fig. 2. Schematic diagram of the Bern3D carbon cycle model. The fully coupled model includes the major global
1219   carbon reservoirs (atmosphere, terrestrial biosphere, ocean, and sediments) and the exchange fluxes between them.
1220   Biogeochemical processes, namely, air-sea gas exchange, biological export production, and particle flux through the
1221   water column, are parameterized by refined OCMIP-2 formulations. Details concerning the model are provided in
1222   Sect. 2 and Appendix A.

1223
1224
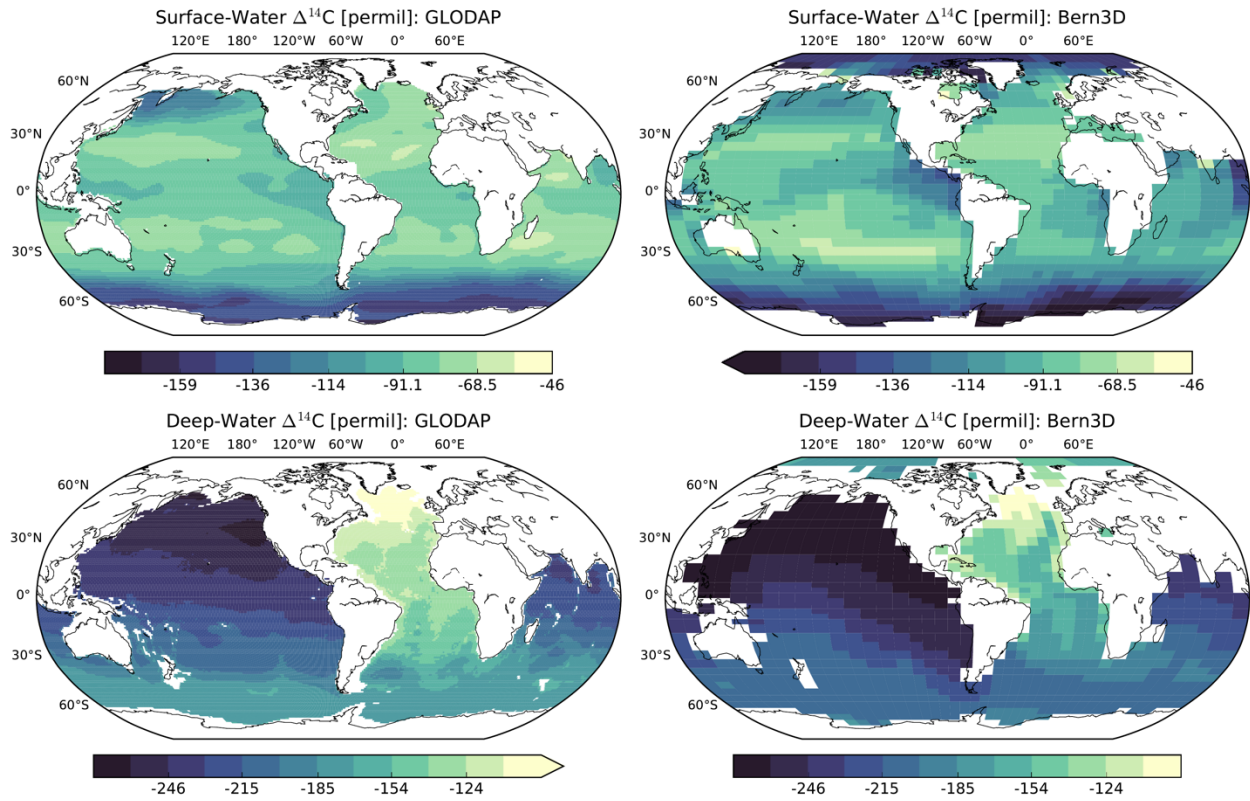
Fig. 3. Steady-state distribution of $\Delta^{14}C$ in the surface (< 100 m) and deep (> 1500 m) ocean for the preindustrial control run (right), compared to the distribution of $\Delta^{14}C$ based on the Global Ocean Data Analysis Project (GLODAP).
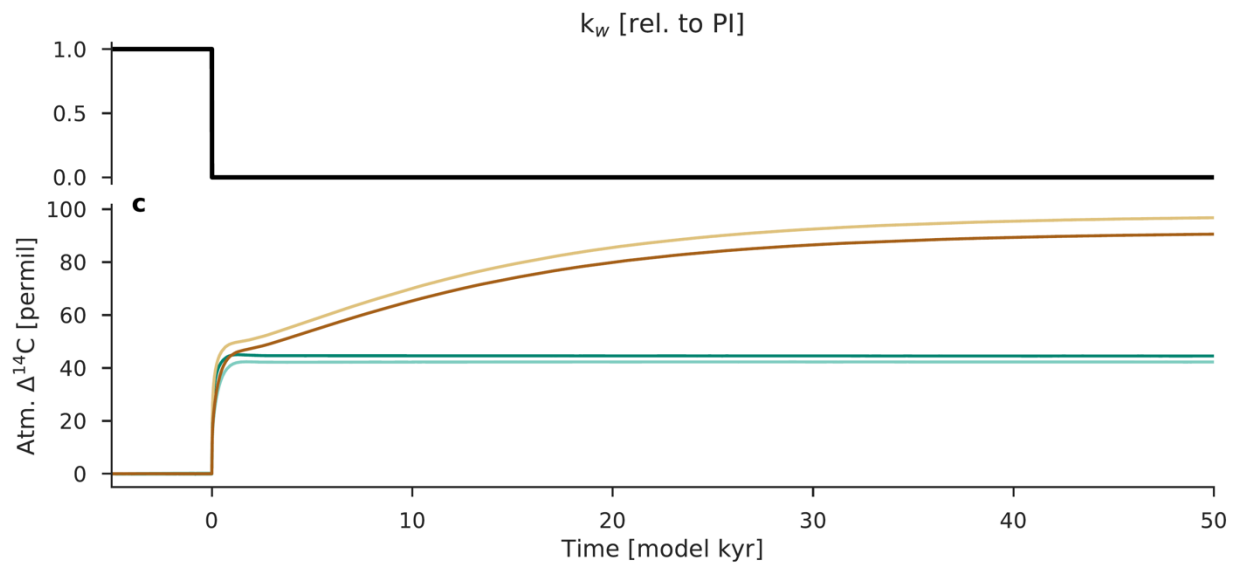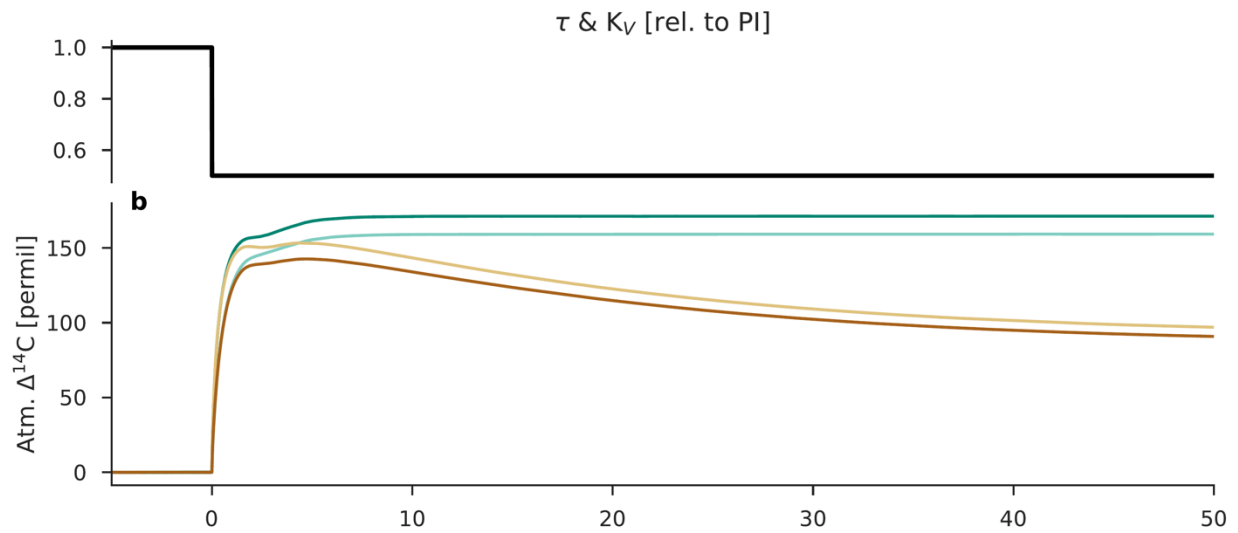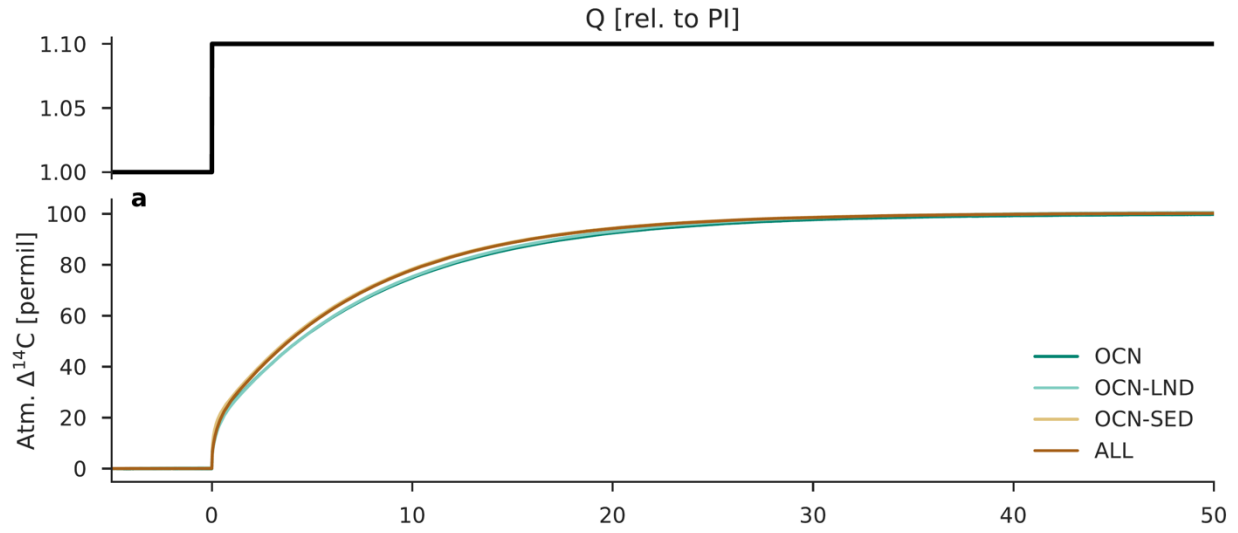
1246 Fig. 4. Response of atmospheric $\Delta^{14}C$ to step changes in ^{14}C production, followed by step changes in the tunable model

1247 parameters of the ocean carbon cycle. (a) ^{14}C production Q is increased at time 0 from 100 to 110 percent of its

1248 preindustrial value ("higher production" scenario). (b) Wind stress scale factor τ and vertical diffusivity K_V are

1249 decreased at time 0 from 100 to 50 percent of their preindustrial values ("reduced deep ocean ventilation" scenario).

1250 (c) Gas transfer velocity k_w is decreased at time 0 from 100 to 0 percent of its preindustrial value at the north ($> 60°N$)

1251 and south ($> 48°S$) poles ("enhanced permanent sea ice cover" scenario). Four model configurations are considered.

1252 The dark turquoise line shows the model results using the atmosphere–ocean (OCN) configuration, the light turquoise

1253 line is the atmosphere–ocean–land (OCN-LND) configuration, the light brown line is the atmosphere–ocean–sediment

1254 (OCN-SED) configuration, and the dark brown line is the atmosphere–ocean–land–sediment (ALL) configuration.

1255
1256
1257
1258
1259
1260
1261
1262
1263
1264
1265
1266
1267
1268
1269
1270
1271
1272
1273
1274

Reduced Deep Ocean Ventilation

Δ Atm. Δ^{14}C [%]

Δ Atm. Inventory [%]

Δ Ocn. Inventory [%]

Δ Sedimentation Flux [%]

Enhanced Permanent Sea Ice Cover

Δ Atm. Δ^{14}C [%]

Δ Atm. Inventory [%]

Δ Ocn. Inventory [%]

Δ Sedimentation Flux [%]

No sediments
Sediments

1275

40
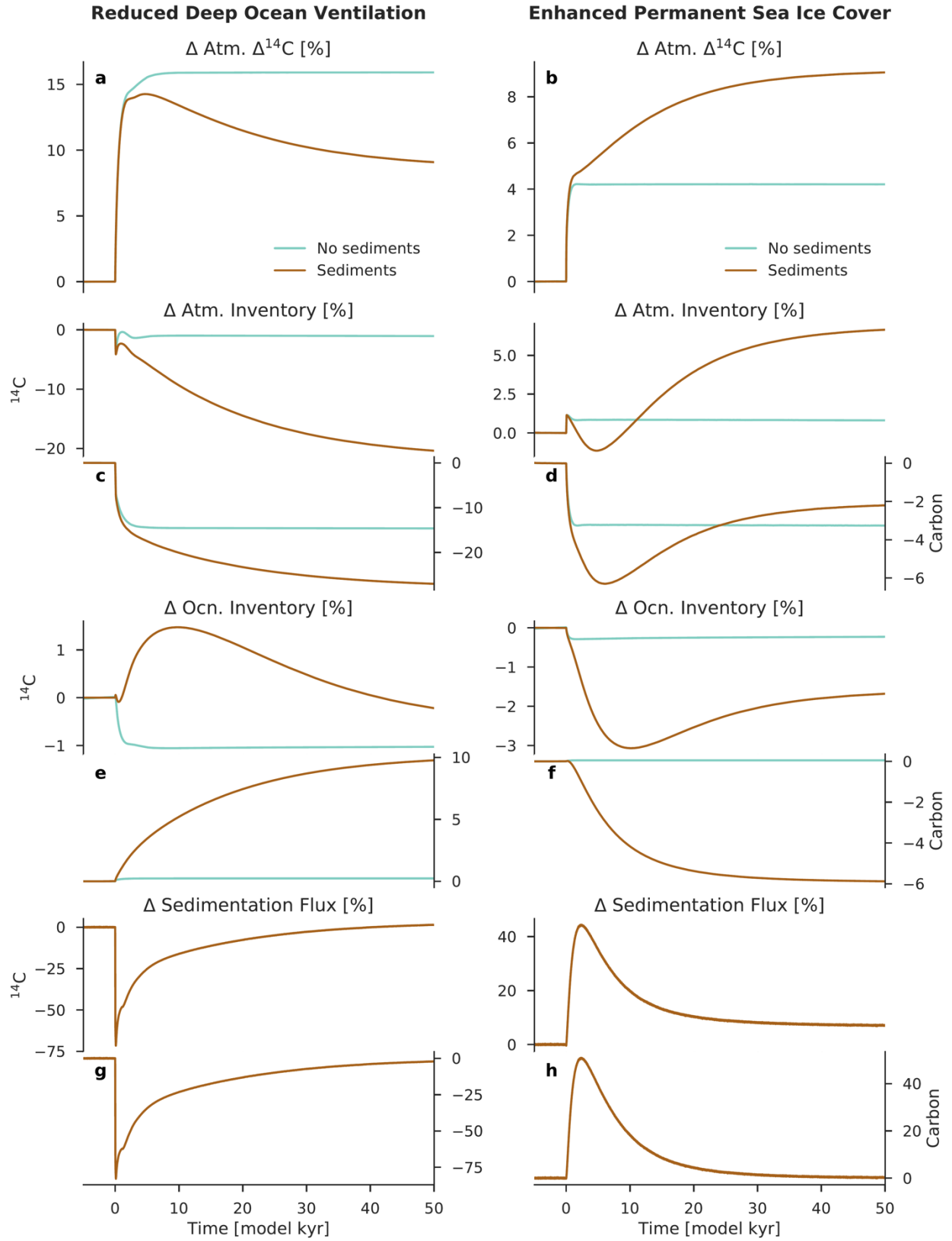
1276   Fig. 5. Changes in carbon reservoir sizes and the sedimentation flux for the scenarios "reduced deep ocean ventilation"

1277   (left) and "enhanced permanent sea ice cover" (right). The change in atmospheric $\Delta^{14}C$ is also shown (a, b). Anomalies

1278   are expressed here as differences relative to the preindustrial steady state (in percent). Turquoise lines show the model

1279   results using configuration OCN-LND (without sediments) and brown lines are configuration ALL (with sediments).

1280   The y-axis on the left-hand side of each panel refers to changes in the ^{14}C inventory, whereas the y-axis on the right-

1281   hand side of each panel refers to changes in the carbon inventory or flux.

1282

1283

1284

1285

1286

1287

1288

1289

1290

1291

1292

1293

1294

1295

1296

1297

1298

1299

1300

1301

1302

1303

1304

1305

1306
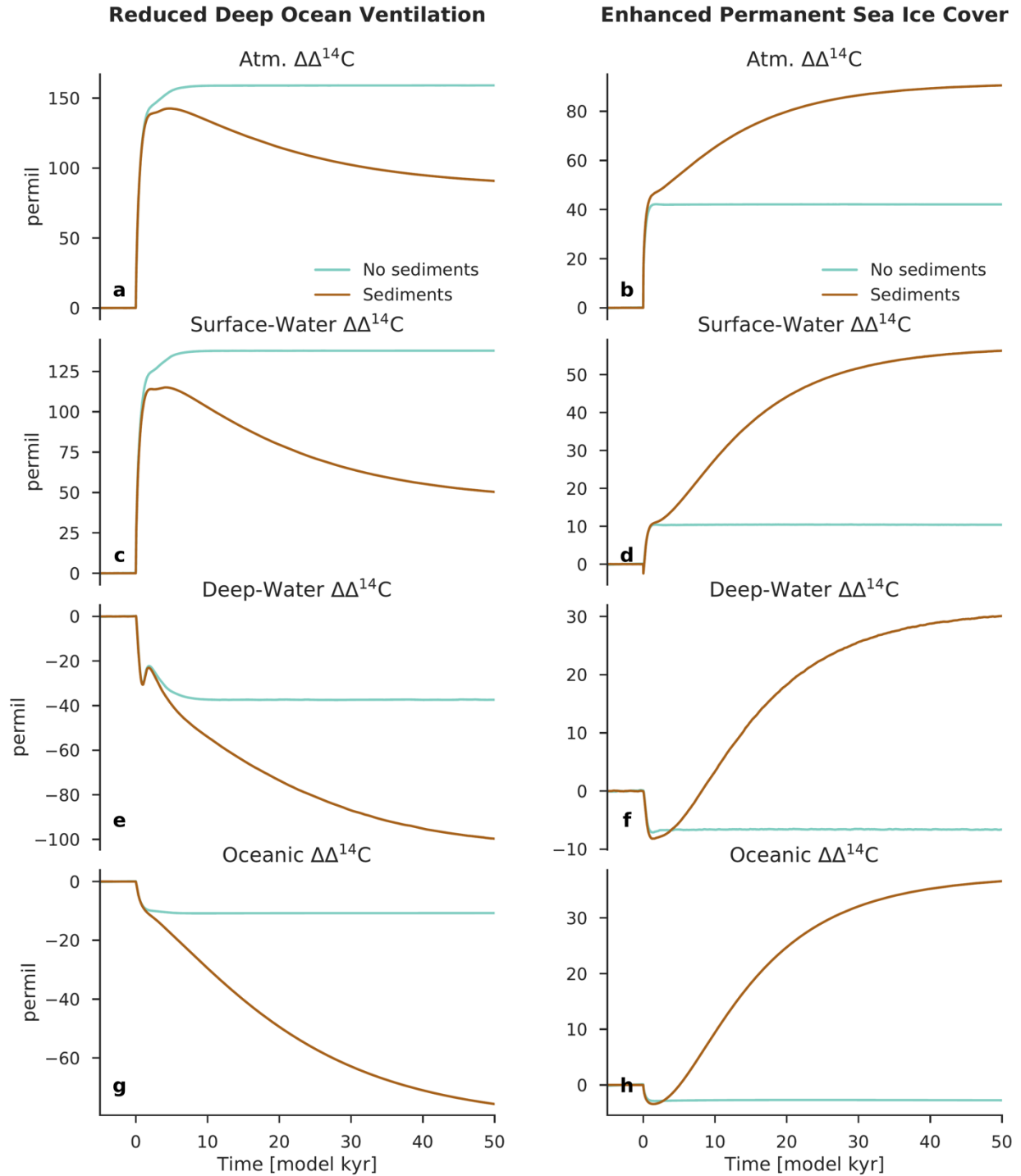
Fig. 6. Change in $\Delta^{14}C$ for the atmosphere, surface ocean, deep ocean, and global ocean for the scenarios "reduced deep ocean ventilation" (left) and "enhanced permanent sea ice cover" (right). Anomalies are expressed here as differences relative to the preindustrial steady state (in permil). Turquoise lines show the model results using configuration OCN-LND (without sediments) and brown lines are configuration ALL (with sediments).

42
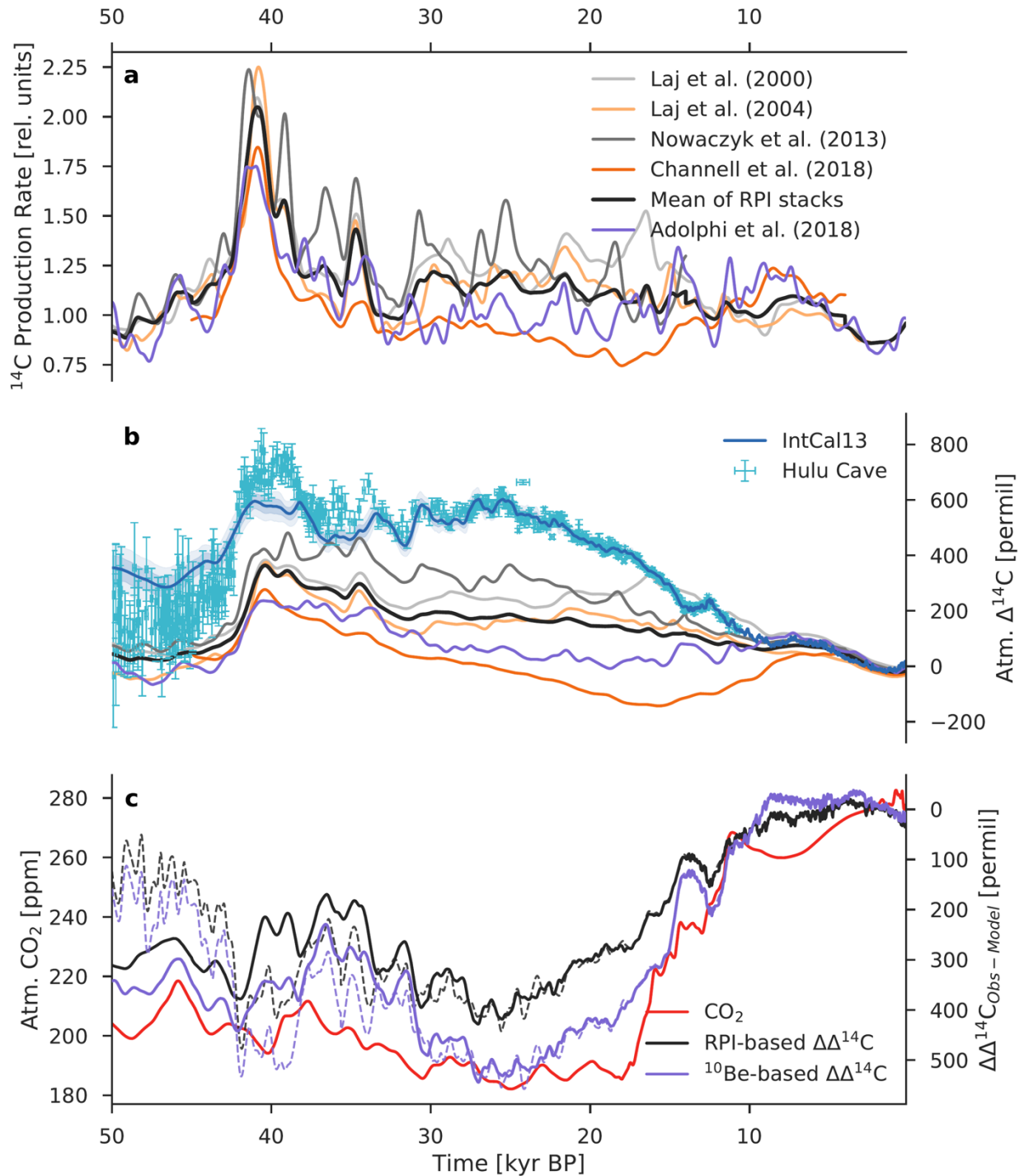
Fig. 7. Component of atmospheric $\Delta^{14}C$ variability caused by production changes alone. (a) Relative ^{14}C production rate as inferred from paleointensity data (gray) and from polar ice-core ^{10}Be fluxes (purple). The heavy dark gray line is the mean paleointensity-based ^{14}C production rate. (b) Modelled $\Delta^{14}C$ records based only on ^{14}C production changes, compared with the reconstructed IntCal13 and Hulu Cave $\Delta^{14}C$ records. The modelled records are given by scenario MOD that assumes a constant preindustrial carbon cycle. (c) Difference between reconstructed $\Delta^{14}C$ and model-simulated $\Delta^{14}C$ using averaged paleointensity data (RPI-based $\Delta\Delta^{14}C$; gray) and the ice-core ^{10}Be data of Adolphi et

1320 al. (2018) (^{10}Be-based $\Delta\Delta^{14}$C; purple), compared with the atmospheric CO_2 record (red). Solid lines show the

1321 IntCal13–model difference, whereas dashed lines show the Hulu–model difference. The $\Delta\Delta^{14}$C curve indicates

1322 changes in Δ^{14}C that can be attributed to some combination of carbon cycle changes, uncertainties in the reconstruction

1323 of the ^{14}C production rate, and uncertainties in the IntCal13 and Hulu Cave Δ^{14}C records.

1324

1325

1326

1327

1328

1329

1330

1331

1332

1333

1334

1335

1336

1337

1338

1339

1340

1341

1342

1343

1344

1345

1346

1347
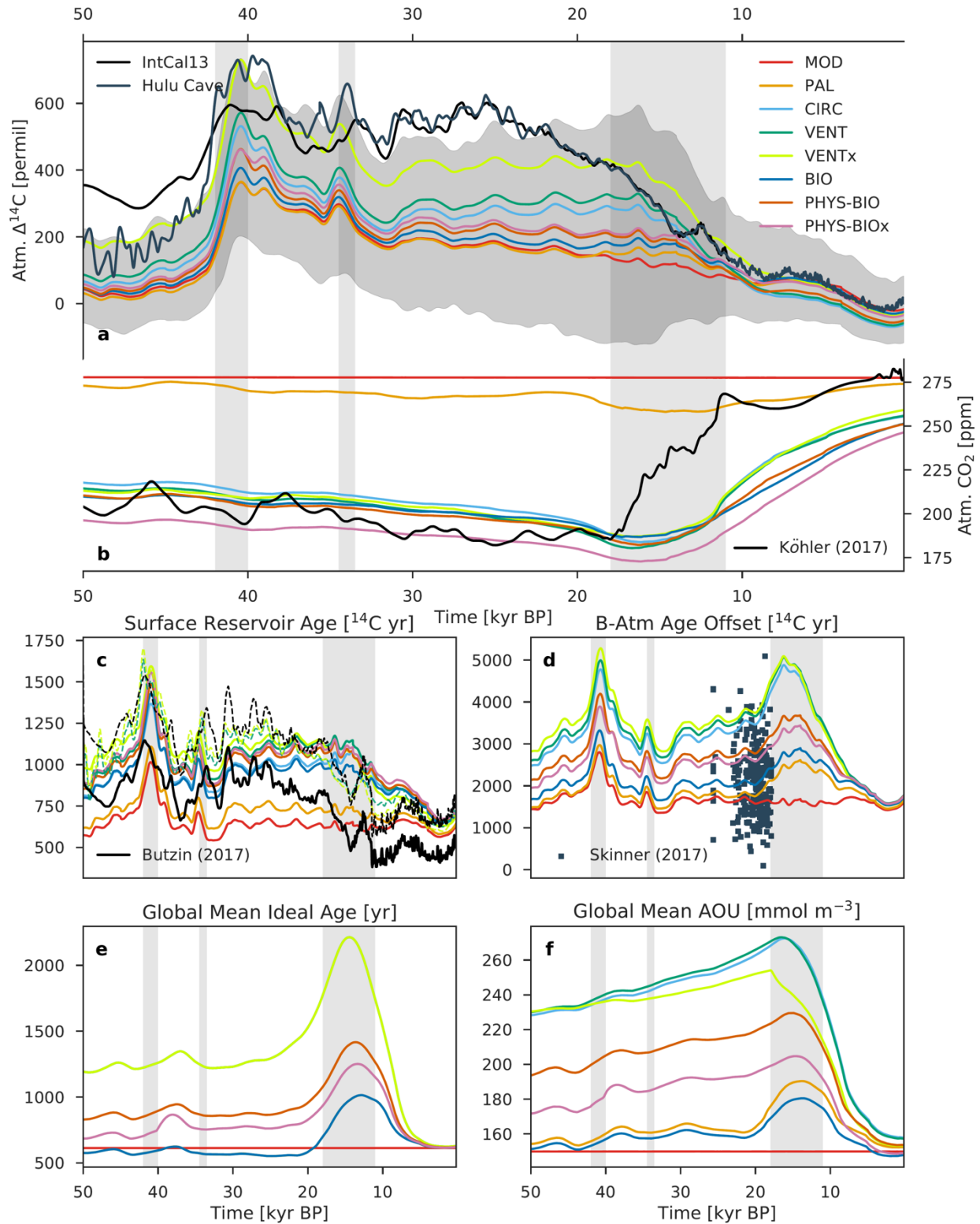
Fig. 8. Modelled records of atmospheric (a) $\Delta^{14}C$ and (b) CO_2, compared with their reconstructed histories (black and dark blue lines). Also shown are modelled records of the global average (c) surface reservoir age and (d) B-Atm ^{14}C age offset, compared with a recent compilation of LGM marine radiocarbon data (dark blue squares) by Skinner et al.

(2017) and model-based surface reservoir age estimates between 50°N and 50°S (solid black line) and across all latitudes (dashed black line) from Butzin et al. (2017), as well as (e) ideal age and (f) apparent oxygen utilization (AOU). Colored lines show the results of model runs using the mean paleointensity-based ^{14}C production rate and the eight different carbon cycle scenarios described in Sect. 2.4 and Table 1. The gray envelope in (a) shows the uncertainty (2σ) from all production rate reconstructions and carbon cycle scenarios, providing a bounded estimate of $\Delta^{14}C$ change. The dashed colored lines in (c) show the surface reservoir age results from VENT and VENTx where atmospheric $\Delta^{14}C$ and CO_2 are prescribed. Radiocarbon ventilation ages are expressed here as radiocarbon reservoir age offsets following Soulet et al. (2016) which are used extensively by the radiocarbon dating community.
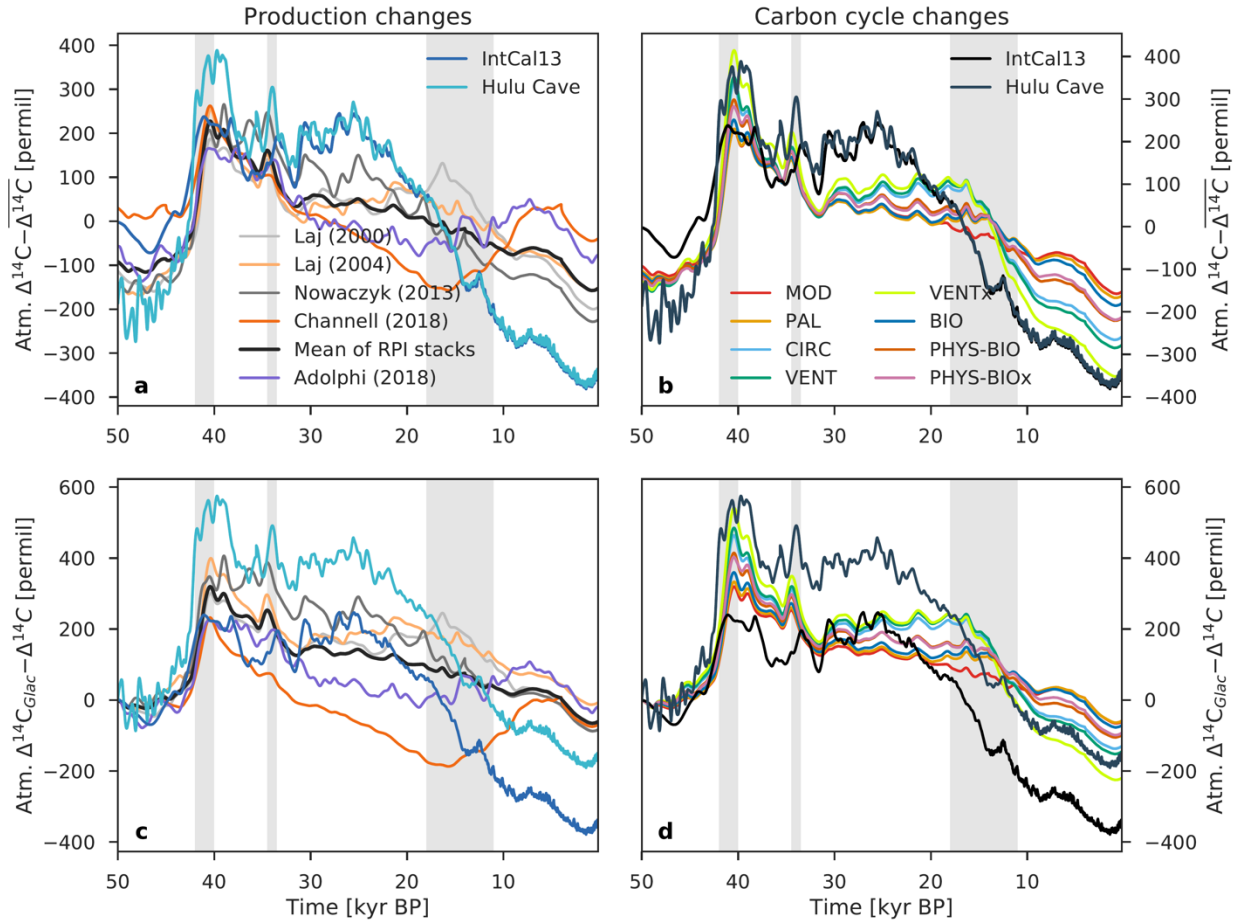
Fig. 9. Comparison of atmospheric $\Delta^{14}C$ variability caused by changes in the ocean carbon cycle (b, d) with production-driven changes in atmospheric $\Delta^{14}C$ using scenario MOD (a, c). For the analysis of carbon cycle changes, only the results of model runs using the mean paleointensity-based ^{14}C production rate are shown. The $\Delta^{14}C$ records in the upper panel (a, b) have been detrended by removing the mean, whereas the lower panel (c, d) shows $\Delta^{14}C$ anomalies expressed as differences relative to the $\Delta^{14}C$ value at 50 kyr BP. Three vertical light gray bars indicate the Laschamp (~41 kyr BP) and Mono Lake (~34 kyr BP) geomagnetic excursions, and the last glacial termination (~18 to 11 kyr BP).
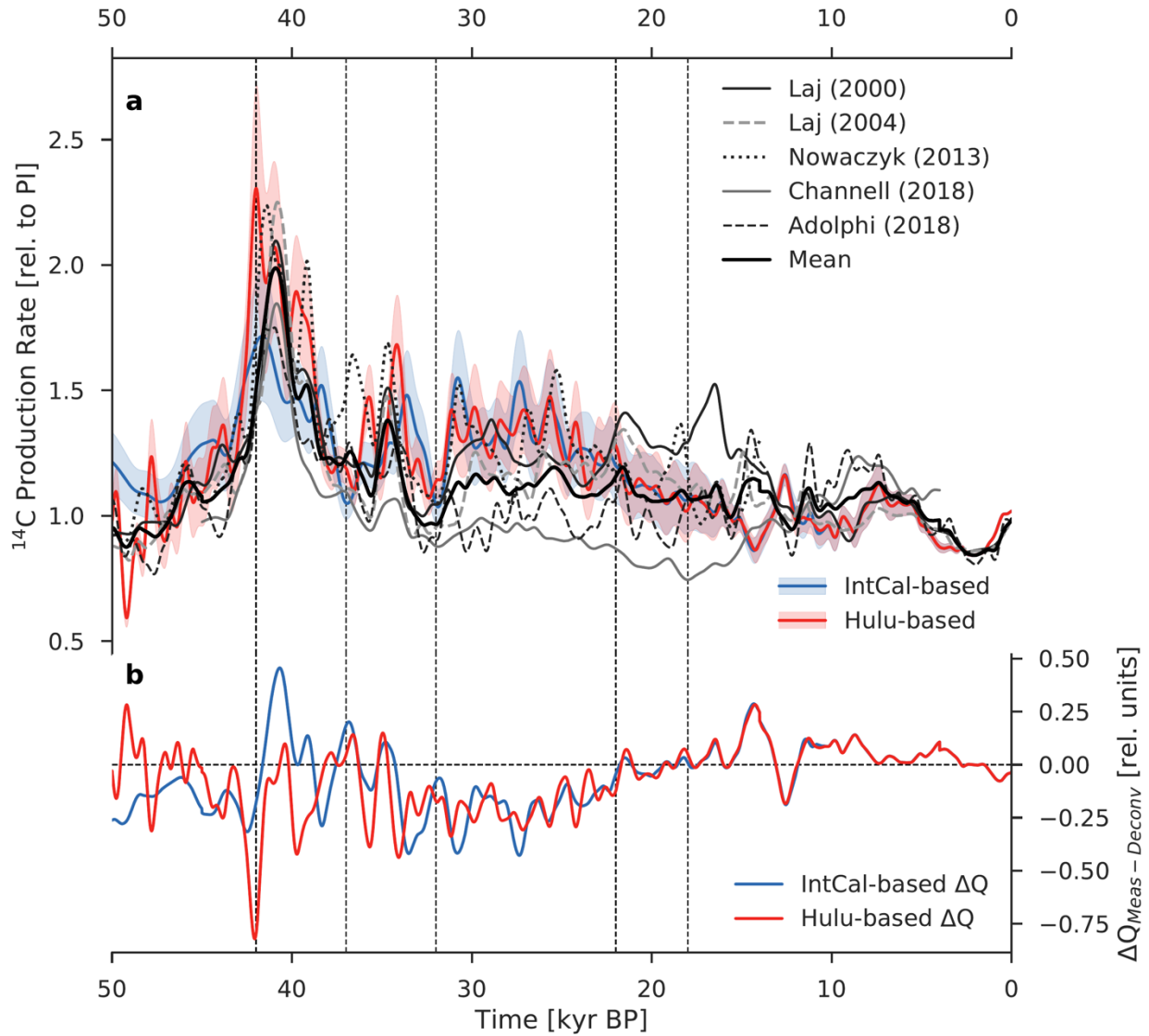
Fig. 10. Comparison of ^{14}C production rate estimates inferred from a deconvolution of the atmospheric Δ^{14}C record and from paleointensity and ice-core ^{10}Be data. (a) ^{14}C production rate calculated as the sum of the modelled air-sea and atmosphere-land $^{14}CO_2$ fluxes and the reconstructed change in the atmospheric ^{14}C inventory and loss of ^{14}C due to radioactive decay (see Eq. [2]). Model-based $^{14}CO_2$ fluxes were obtained by forcing the Bern3D carbon cycle model with reconstructed variations in atmospheric Δ^{14}C and CO_2 as well as seven different carbon cycle scenarios. Results of model runs using the IntCal13 calibration curve are shown in the light blue envelope (2σ), whereas the light red envelope (2σ) shows the results from simulations using the composite Hulu Cave (10.6 to 50 kyr BP) and IntCal13 (0 to 10.6 kyr BP) Δ^{14}C record. The heavy black line is the mean of five available production rate reconstructions: Laj et al. (2000), Laj et al. (2004), Nowaczyk et al. (2013), Channell et al. (2018), and Adolphi et al. (2018). (b) Difference between the mean of the measurement-based production rate estimates (heavy black line) and estimates based on the deconvolution of the IntCal13 (IntCal-based ΔQ; blue) and Hulu Cave (Hulu-based ΔQ; red) Δ^{14}C data.
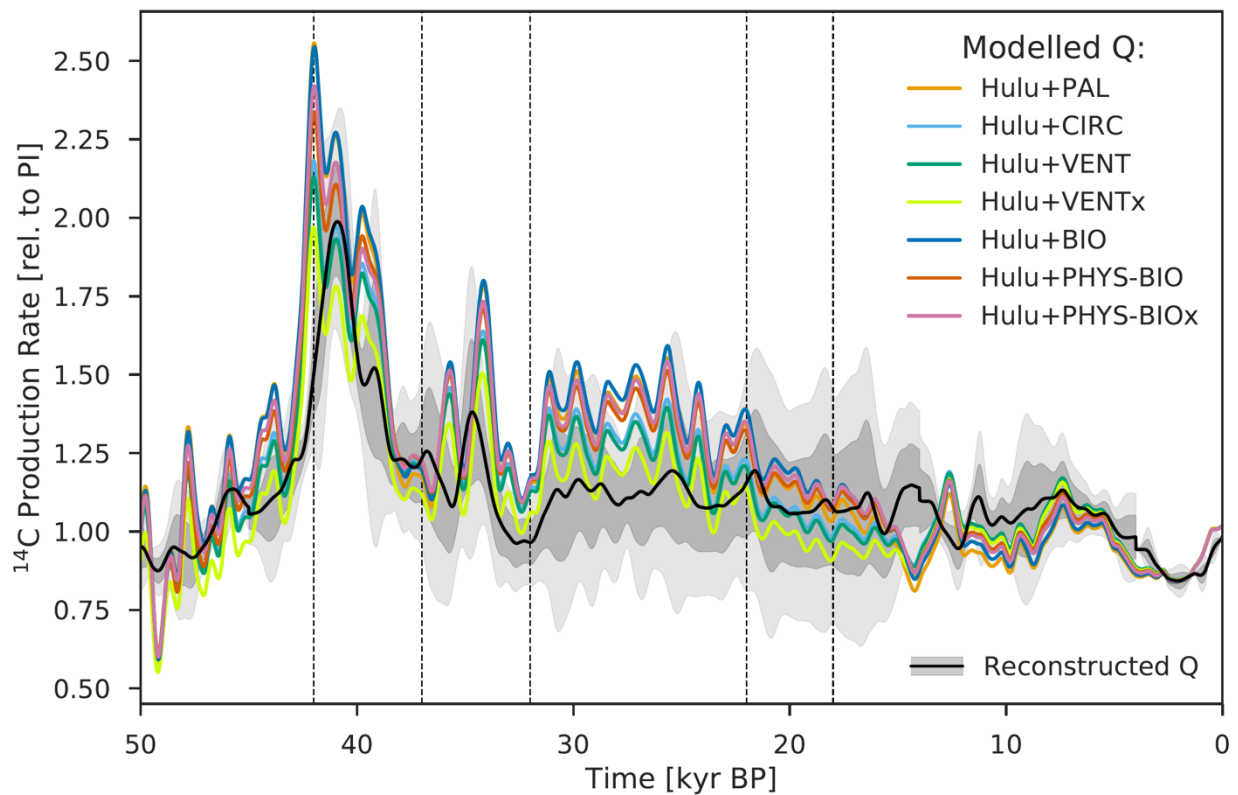
1413

1414 Fig. 11. Relative ^{14}C production rate as inferred from the Bern3D model under seven carbon cycle scenarios (see Sect.

1415 2.4). Estimates shown here are based on the composite Hulu Cave and IntCal13 Δ^{14}C record. The black line is the

1416 mean of the five production rate reconstructions shown in Fig. 10; the gray envelope shows its uncertainty (2σ).

1417

1418

1419

1420

1421

1422

1423

1424

1425

1426

1427

1428

1429

1430

1431